On the formation of highly active Ziegler-Natta catalysts clarified by a multifaceted characterization approach

Alessandro Piovano,[,**,†,‡] Toru Wada,[**,‡,§] Alessia Amodio,[†] Gentoku Takasao,[§] Tomohiro Ikeda,[§] Zhu Dongzhi,[§] Minoru Terano,[‡,§] Chammingkwan Patchanee,[‡,§] Elena Groppo,[†,‡] and Toshiaki Taniike[*,‡,§]*

* *Corresponding authors*

** *These two authors contributed equally to this work, and both are cited as first authors.*

[†]Department of Chemistry, INSTM and NIS Centre, University of Torino, Via Giuria 7, 10125 Torino, Italy

[‡]Dutch Polymer Institute, P.O. Box 902, 5600 AX Eindhoven, the Netherlands

[§]Graduate School of Advanced Science and Technology, Japan Advanced Institute of Science and Technology, 1-1 Asahidai, Nomi, Ishikawa, 923-1292, Japan

KEYWORDS: Ziegler-Natta catalysts, electronic properties, morphology, IR spectroscopy, synchrotron, total scattering, XRD, pair distribution function

ABSTRACT

Although the formation of nanosized and defective δ-$MgCl_2$ is essential for the performance of Ziegler-Natta catalysts, the process has not sufficiently been elucidated due to certain limitations in characterization. Here, the formation of nanostructures and active surfaces of Ziegler-Natta catalysts were investigated in detail based on a multifaceted set of characterization techniques represented by X-ray total scattering and various spectroscopies, in correlation with chemical composition analysis and polymerization tests. Solid samples were extracted in the course of the catalyst preparation from $Mg(OEt)_2$, and subjected to the analysis. Several interesting results were found. The addition of $TiCl_4$ almost spontaneously converts $Mg(OEt)_2$ into $MgCl_2$ seeds mainly exposing the {001} basal surface, whose dimensions are below 2 nm; a large Ti amount stays on the material as physisorbed 4-fold coordinated $TiCl_x(OEt)_{4-x}$ species. The heating treatment removes the physisorbed $TiCl_x(OEt)_{4-x}$ and/or convert them into chemisorbed 6-fold coordinated $TiCl_x(OEt)_{4-x}$, while the subsequent addition of an internal donor (here dibutyl phthalate, DBP) promotes a substantial reconstruction and growth of $MgCl_2$ seeds to almost the same size as the final catalyst (ca. 6 nm), with the exposure of the more catalytically relevant lateral surfaces. DBP is in one part adsorbed on $MgCl_2$ surfaces and in the other part complexed with Ti sites. This complex is only partially removed in the following steps of the synthesis. The second $TiCl_4$ addition replaces the chemisorbed $TiCl_x(OEt)_{4-x}$ with 6-fold coordinated $TiCl_4$ species, but it also causes side reactions with DBP, as testified by the formation of phthaloyl chloride (POC). After activation by triethylaluminum (TEAl), the activity per Ti for ethylene was almost constant throughout the whole preparation process after the initial $TiCl_4$ addition, whereas the activity for propylene was negligible before the addition of the donor and increased dramatically in the subsequent steps of the preparation. This was further investigated based on spectroscopies for TEAl-activated samples, in order to individuate the active Ti species responsible for the catalysis and to monitor the fate of DBP

upon TEAl reaction. The multifaceted characterization approach allowed us to integrate information on the formation of δ-$MgCl_2$, their surfaces, and adsorbed species, providing us with deep insights into the meaning of each step within an industrial catalyst preparation method that has been empirically refined over a long history.

1. INTRODCUTION

After almost seventy years since Karl Ziegler and Giulio Natta broke the monopoly of Nature on the synthesis of stereoregular polymers, Ziegler-Natta (ZN) catalysts are nowadays responsible for 99% of the world polypropylene (PP) production as well as one fourth of that of high-density polyethylene (HDPE).[1] The economic turnover of this industrial process brushes the verge of 300 billion dollars in 2020 and is forecasted to still grow at a compound annual growth rate of 6 % in the next decade.[2]

From their original and quite simple composition, ZN catalysts have evolved along several generations characterized by a gradually improved activity and stereoselectivity, up to the current multi-component composition: $TiCl_4$ (the active phase) is dispersed with organic Lewis bases (the internal donors) on $MgCl_2$ (the support material) and activated by AlR_3 (the co-catalyst), together with other organic Lewis bases (the external donors).[3-6] The internal/external donors are considered to be located at the vicinity of the Ti active species and to improve stereospecificity through steric hindrance. Such complex composition allows, by means of catalyst design, finely controlling the structure of the produced polymer across multiple scales, from the molecular architecture of the polymer chains to its distribution critical for actual properties, and finally to the morphology of the polymer particles.

In industrial practice, two main routes have been developed to integrate $TiCl_4$, $MgCl_2$, and an electron donor into a single solid material, usually called pre-catalyst.[3] Note that the electron donor in the pre-catalyst is termed as internal donor to distinguish it from the external one, which is added directly in the reactor along with the AlR_3 activator. The former route (traditional) is based on the mechanical ball-milling of highly crystalline $MgCl_2$ (α form) with the internal donor and/or $TiCl_4$.[7-13] The latter route (advanced) employs the chemical transformation of a $MgCl_2$-precursor into nanostructured and highly defective $MgCl_2$ (δ form) by $TiCl_4$ itself in the presence of the donor,[14-29] and generally leads to more disordered and more active nanostructures.[30-32] In a typical chemical preparation route, all the components are intimately connected to each other. $TiCl_4$ promotes the chlorination of the precursor into $MgCl_2$ and exerts a capping effect on the newly formed $MgCl_2$ nanoparticles.[33] The electron donor not only influences the $MgCl_2$ morphology by stabilizing specific surfaces,[20, 22] but also interacts with the Ti sites through direct coordination[34-37] or more plausibly through coadsorption.[38] By-products formed during the chlorination must not be overlooked as these products could adsorb on $MgCl_2$ surfaces, and work as catalytic poisons unless properly removed.[39]

All the above-mentioned events parallel in the catalyst preparation to determine the final structure of ZN catalysts at multiple length scales and, in turn, the catalyst performance. Therefore, monitoring the evolution of the catalysts along the synthesis is the only way to elucidate all the inter-connections between their components, laying the groundwork for a future rational design of new and more efficient catalytic systems. In this work, we focus on the ZN catalyst obtained from a $Mg(OEt)_2$ precursor, using dibutyl phthalate (DBP) as an internal donor. The $Mg(OEt)_2$-based ZN catalysts are among one of the most employed catalysts in industrial PP production, because of their high activity and stereoselectivity. The difficulties of this investigation rely not only on the chemical lability or air sensitivity of samples, but also on the multi-technique approach needed to face such a multi-scale

complexity, ranging from the local structure of the Ti sites to the textural properties of $MgCl_2$ particles. Only a few pioneering works in the literature dealt with the evolution of the material during the ZN catalyst synthesis from $Mg(OEt)_2$, where a series of samples were extracted from the reactor, and characterized for their chemical composition, structure, and activity.[40-42] According to Jeong et al., the activity towards propylene polymerization increases linearly with the increase in the number of $TiCl_4$ addition, while the presence of an internal donor affects drastically the stereospecificity of the catalyst (enhancing the isotacticity of the produced PP from less than 50 % up to 95 % in *mmmm*).[40] More in details, Chumachenko et al. found out that the reaction at early stages between $Mg(OEt)_2$ and $TiCl_4$ leads to a mixture of $MgCl_2$ and $TiCl_3(OEt)$ with very high surface area (415 m^2/g) but low activity and stereospecificity, while the subsequent addition of DBP causes the removal of inactive $TiCl_3(OEt)$, the growth of $MgCl_2$ crystallites (the surface area decreases to 211 m^2/g), and a significant increase of the overall activity and stereospecificity.[42] Finally, Kim et al. mostly focused on the mutual reactions between $Mg(OEt)_2$, $TiCl_4$ and the benzoyl chloride (BzCl) used as an electron donor or its precursor, demonstrating the high interchangeability of $(OEt)^-$ and Cl^- anionic ligands.[41]

Recently, we proposed a combination of cutting-edge characterization techniques to clarify the identity of δ-$MgCl_2$, which includes X-ray total scattering for defining the nano-sized and disordered structure,[30] and vibrational spectroscopies for determining the exposed surfaces and their relative extension.[43] In this study, the same approach has been adopted, but complemented by chemical analysis, polymerization tests and UV-Vis spectroscopy, in order to elucidate the chemical reactions and structural evolution taking place during the ZN catalyst preparation.

2. EXPERIMENTAL

2.1. Reagents

Mg powder was purchased from Merck, KGaA. Ethanol (purity > 99.5%, Kanto Chemical) was dried over 3A molecular sieve with N_2 bubbling. Iodine (I_2, purity > 99.999%, FUJIFILM Wako Pure Chemical) was used as a halide initiator. *n*-Heptane (purity > 99.5%,), toluene (purity > 99.5%), and di-*n*-butylphthalate (DBP, purity > 98%) were purchased from FUJIFILM Wako Pure Chemical and dried over 4A molecular sieve with N_2 bubbling. Triethylaluminium (TEAl) was donated by Tosoh Finechem. Cyclohexylmethyldimethoxysilane (CMDMS) was purchased from Sigma-Aldrich and purified by vacuum distillation. Propylene was donated by Japan Polychem Corp., and ethylene was purchased from Sumitomo Seika Chemicals Co., Ltd.

2.2. Catalyst Synthesis

All the manipulations and storage were performed under a N_2 atmosphere to prevent moisture contamination. The starting material, $Mg(OEt)_2$, was synthesized according to a previously reported method.[44-46] Briefly, 2.64 mmol of I_2 and 25.0 g of ethanol were introduced to a 500 mL jacket-type flask equipped with a mechanical stirrer rotating at 180 rpm. After dissolving I_2 in ethanol at 75 °C, 2.5 g of Mg powder and 25.0 g of ethanol were added. The same amount of Mg powder and ethanol were repeatedly added with sufficient intervals between individual additions. The total amount of Mg powder and ethanol were 25.0 g and 125 g. The resultant solid product was recovered by washing with 200 mL of ethanol and dried in vacuo at below 40 °C.

The procedures for catalyst preparation and sampling are shown in Scheme 1. A three-necked flask (500 mL) equipped with a mechanical stirrer and purged with N_2 was charged with 20 g of $Mg(OEt)_2$ powder and 136 mL of toluene. 20 mL of $TiCl_4$ was dropwise introduced by keeping the temperature of the mixture below –5 °C. The mixture was gradually heated, and when the temperature reached 60 °C, 4.3 mL of DBP was dropped in the flask. The mixture

was further heated, and kept at 110 °C for 2 hours. The solid product in the flask was washed with toluene twice by a decantation method, and then 16 mL of $TiCl_4$ and 68 mL of toluene were introduced. The mixture was heated and aged at 110 °C for 4 hours. Note that the aging time after the second addition of $TiCl_4$ is usually set to 2 hours, while the duration was extended to 4 hours in this study for the sake of characterization. Finally the mixture was sufficiently washed with toluene and *n*-heptane to obtain the catalyst. At several key points in the above preparation, samples were extracted from the flask using a syringe. The amount of each extraction corresponded to ca. 3 g of solid. The extracted solid was washed thoroughly with *n*-heptane, dried in vacuum at 80 °C, and stored under N_2 for characterization. The timing of the extraction and the corresponding sample codes are as follows: (**A**) after the first $TiCl_4$ addition, (**B**) immediately before the addition of DBP, (**C**) when the temperature of the mixture reached 110 °C, (**D**) after being kept at 110 °C for 2 hours, (**E**) after 2 hours of the aging, and (**F**) the final catalyst. All the extracted samples were adequately washed with dehydrated *n*-heptane and then dried in vacuum at 80 °C.

Scheme 1. Schematic description of the main steps upon ZN catalyst preparation, with indication of sampling points.

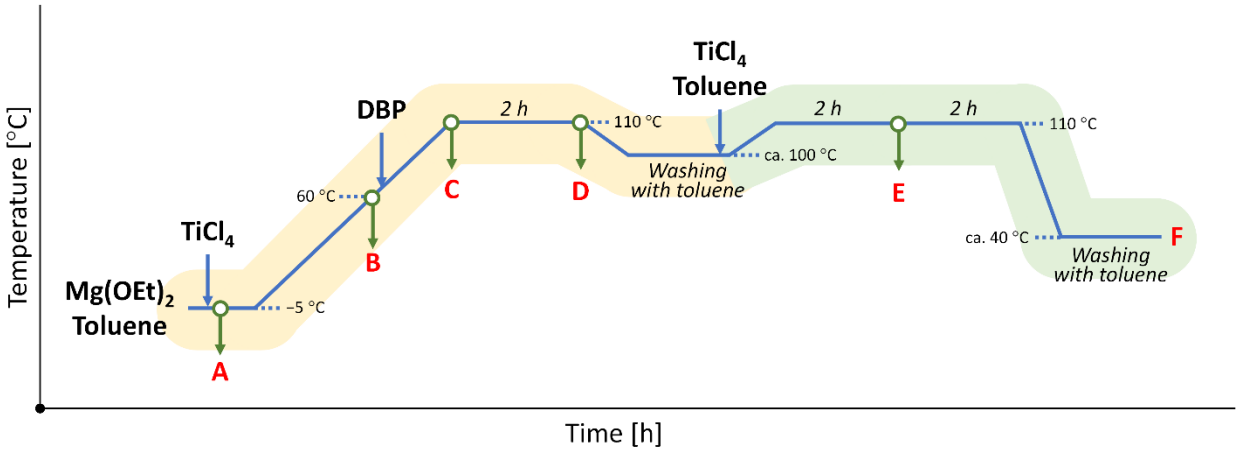

157

158

159 **2.3. Ethylene and Propylene Polymerization**

160 Polymerization tests were carried out in semi-batch mode. A mechanically stirred 1 L
161 autoclave reactor was charged with 300 mL of heptane and 3.0 mmol of TEAl for ethylene
162 polymerization, or with 300 mL of heptane, 3.0 mmol of TEAl, and 0.30 mmol of CMDMS
163 for propylene polymerization. Either ethylene or propylene was introduced to the reactor and
164 saturated at 0.4 MPa and 70 °C. The polymerization was initiated by the injection of a catalyst
165 (10–50 mg) into the reactor and continued for 30 minutes, where the temperature, the monomer
166 pressure, and the stirring speed were maintained at 70 °C, 0.4 MPa, and 500 rpm, respectively.
167 The obtained polymer powder was recovered by filtration and vacuum drying at 60 °C for 6
168 hours.

169

170 **2.4. Catalysts Activation by TEAl**

171 In order to investigate the activation process, some selected samples (**A**, **B**, **C**, and **F**) were
172 separately reacted with TEAl. The activation of the catalysts was carried out in glove-box by
173 impregnating at room temperature the powders with TEAl (diluted 10 v/v % in hexane) at an
174 Al:Ti ratio of 2:1. Afterwards, the solvent was removed by degassing under vacuum.

175

176 **2.5. Characterization**

2.5.1. Chemical Composition

The chemical composition of the samples was analyzed as follows. The Ti content was measured by a colorimetric method, where ca. 50 mg of a sample was dissolved in an aqueous solution of HCl/H_2SO_4, and then H_2O_2 solution was added to develop the color. The absorption intensity of the band at 410 nm was recorded on a UV–vis spectrometer (V-670 JASCO), which was used to calculate the titanium content based on external calibration.[44] Organic contents were analyzed by ^1H NMR on a Bruker AVANCE III 400 MHz spectrometer according to our previous study.[39] 10–30 mg of a sample was dissolved in 0.7 mL of DMSO-d_6 with 40 μg of 1,1,2,2-tetrachloroethane as an internal standard. The morphology of the catalyst particles was observed by scanning electron microscopy (SEM, Hitachi Ltd., S-4500). In order to minimize the risk of moisture contamination during sample transfer, sputter coating was omitted. The acceleration voltage was set to 1 kV to suppress a charge-up effect.

2.5.2. Polymer Characterization

The obtained polymers were subjected to differential scanning calorimetry (DSC, Mettler Toledo DSC 822) under a nitrogen atmosphere. About 8 mg of polymer in an aluminum pan were heated to 230 °C and then cooled down to 25 °C (20 °C min^{-1}). The cooled sample was then heated up to 230 °C at a heating rate of 20 °C min^{-1} to determine the melting temperature (T_m) and the crystallinity (X_c) from the melting endotherm.

Gel permeation chromatography (GPC, Tosoh Co., HLC-8321GPC/HT) measurements were performed at 140 °C using *o*-dichlorobenzene as a mobile phase. Polystyrene standards were used for calibration.

2.5.3. X-ray Total Scattering

X-ray total scattering data were acquired at the BL04B2 of SPring-8 (Hyogo, Japan). Each sample in the powder form was filled in a quartz glass capillary with a diameter of 2 mm and a wall thickness of 0.01 mm, placed in a vacuum chamber, and irradiated with the X-ray beam at an energy of 61.4 keV (λ=0.202 Å). The diffraction patterns were recorded in transmission mode and in the horizontal scattering plane by using solid-state array detectors. The upper limit of the scattering vector (Q) was 25.7 $Å^{-1}$. The measured X-ray scattering data were corrected for polarization, absorption, and background. The contribution of Compton scattering was subtracted using standard analysis procedures.[47] The calculated total structure factor $S(Q)$ was converted into reduced pair distribution function (PDF) $G(r)$ via Fourier transformation with a Lorch modification function.[48]

2.5.4. IR Spectroscopy

IR spectra were collected with a Bruker Vertex70 FT-IR spectrophotometer, equipped with a DTGS detector for the Far-IR region and a MCT detector for the Mid-IR region (hereafter generically referred to as IR).

For the Far-IR measurements, the samples were prepared directly inside a N_2-filled glove-box as thin layers deposited on a highly pure Si wafer (from a suspension in hexane), and placed inside a quartz cell with PE windows, allowing to measure the spectra without exposing the samples to air. Far-IR spectra were acquired at a resolution of 4 cm^{-1}, and are shown after subtracting the weak contributions of both the Si wafer and the PE windows.

For the IR measurements, the samples were diluted in anhydrous KBr, compressed in the form of thin self-supporting pellets (with a resulting density of 10 mg of sample per cm^2) inside the glove-box, and placed inside a quartz cell with KBr windows. The IR spectra were acquired at a resolution of 2 cm^{-1}. The curve fitting of the spectra in the ν(C=O) region was carried out by OPUS software (Bruker), imposing the Gaussian shape to the contributions.

2.5.5. DR UV-Vis Spectroscopy

UV-Vis spectra were collected in diffuse reflectance mode (DR), with a Varian Cary5000 spectrophotometer, equipped with a reflectance sphere. The powder samples were directly placed inside a bulb-shaped cell made of optical quartz (Suprasil) within the glove-box, and successively measured in N_2 atmosphere. The spectra have been collected in reflectance mode and then converted in the Kubelka-Munk function.

3. RESULTS AND DISCUSSION

In this study, we performed a multi-faceted characterization of solid samples extracted at different steps of catalyst preparation for addressing two key questions: 1) how catalyst nanostructures are generated and shaped during the preparation, and 2) which are the mutual interactions between all the catalyst components. The structure of the Section is as follows: in Section **3.1** the chemical composition of all the samples is discussed; Section **3.2** describes the performances of each intermediate as well as of the final catalyst in olefin polymerization after activation by TEAl; then the results of individual characterization methods are explained and discussed in Sections **3.3-3.6**, and finally all the results are combined to give a conclusive picture in Section **4**.

3.1. Chemical Composition

The evolution of the chemical composition along the ZN catalyst synthesis is summarized in Table 1. In general, it has been reported that $Mg(OEt)_2$ is chlorinated by $TiCl_4$ to produce $MgCl_2$ and $TiCl_x(OEt)_{4-x}$. The OEt group remains in the catalyst to a greater or lower extent due to both/either incomplete chlorination of $Mg(OEt)_2$ and/or persistence of surface $TiCl_x(OEt)_{4-x}$ species, which greatly reduces the activity and stereospecificity of the catalyst.

Here, the OEt group was quantified by the methylene peak in ^{1}H NMR, so the OEt residual can be associated to either $Mg(OEt)_2$ or $TiCl_x(OEt)_{4-x}$. Initially (**A**,**B**), the Ti content is pretty high (about 2.5 mmol g^{-1}) and the Ti:OEt molar ratio is about 1:1. By introducing DBP and heating up to 110 °C, the Ti content is reduced to less than half (**C**), and to a further half by the aging (**D**), whereas the Ti:OEt molar ratio is kept almost constant. Hence, it is plausible that in the early stages of catalyst preparation, Ti is present almost exclusively as $TiCl_3(OEt)$. Heating with DBP causes a reduction in the amount of $TiCl_3(OEt)$. The second $TiCl_4$ treatment has almost no impact on the Ti content (**E**,**F**), but the OEt further decreases to below 0.2 mmol g^{-1}, suggesting that $TiCl_x(OEt)_{4-x}$ species are replaced by $TiCl_4$. Concerning DBP, its content at the end of ZN catalyst synthesis (**F**) converges to about 0.6 mmol g^{-1}, which corresponds to a molar amount comparable to that of Ti. Finally, it is worth noticing that in ZN catalysts containing DBP as an internal donor, phthaloyl chlorides (POC) are known as typical by-products, which are produced by a reaction of DBP and $TiCl_4$ at an elevated temperature. In our analysis, POC were not observed during the first $TiCl_4$ treatment (**C**,**D**), but was slightly observed (column Cl in Table 1) after the second $TiCl_4$ treatment (**E,F**), which suggests that the fresh $TiCl_4$ is more reactive towards the surface adsorbates.

Table 1. Evolution in the chemical composition along the synthesis steps.

Sample	Ti [a] [mmol g^{-1}]	OEt [b] [mmol g^{-1}]	Pthalate [b,c]			
			n-Bu [mmol g^{-1}]	Et [mmol g^{-1}]	Cl [mmol g^{-1}]	Phthalate (total) [mmol g^{-1}]
A	2.42	2.09				
B	2.53	2.49				
C	1.07	0.89	1.70	0.09	n.d. [d]	0.89
D	0.56	0.47	0.97	0.56	n.d. [d]	0.77

E	0.63	0.18	0.73	0.48	0.03	0.63
F	0.56	0.18	0.68	0.46	0.04	0.61

[a] Determined by titration.

[b] Determined by ^{1}H NMR.

[c] The *n*-Butoxy groups of DBP is known to be substituted by ethoxy groups as well as chlorine atoms during catalyst preparation. The total phthalate amount was calculated as half of the total amount of possible substitutional groups: (*n*-Bu + Et + Cl)/2.

[d] Not detected.

3.2. Performance in Olefin Polymerization

Samples **A**–**F** have been used as catalysts for ethylene and propylene homopolymerization after activation by TEAl. Table 2 summarizes the activity data, while Figure 1 shows the activity normalized per Ti-mol. The reactivity is completely different for the two monomers, suggesting that the composition and structural features required for ethylene and propylene polymerization are completely different. The ethylene polymerization activity (per Ti-mol) was almost constant throughout the catalyst synthesis, i.e. insensitive to the composition and structural features. In contrast, propylene polymerization was found to be sensitive to the stage of the catalyst preparation: no polymer was obtained before DBP was added and heated up to 110 °C (**A**,**B**), but then the activity increased significantly along with the synthesis. The characterization of all the produced polymers is summarized in Table S1 and Figure S1.

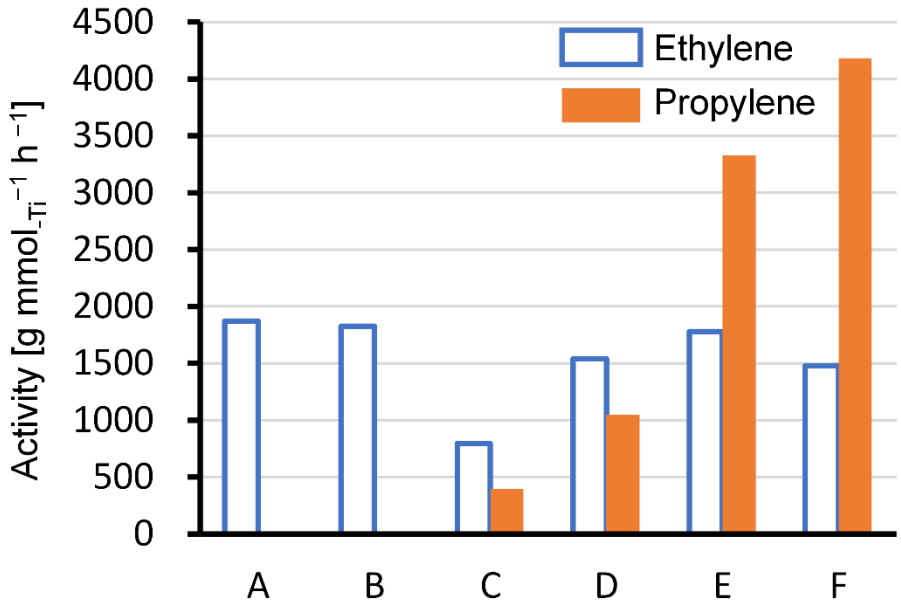

Figure 1. Ethylene and propylene polymerization activity of the samples extracted at different stages in the course of catalyst preparation. Reaction conditions: monomer pressure = 0.4 MPa, catalyst = 10–50 mg, *n*-heptane = 300 mL, TEAl = 3.0 mmol, 70 °C, 30 min, CMDMS (for propylene polymerization) = 0.30 mmol.

Table 2. Evolution of the activity towards ethylene and propylene polymerization.

Sample	Activity in ethylene polym.		Activity in propylene polym. [a]	
	[g$_{-PE}$ g$_{-cat}^{-1}$ h^{-1}]	[g$_{-PE}$ mmol$_{-Ti}^{-1}$ h^{-1}]	[g$_{-PP}$ g$_{-cat}^{-1}$ h^{-1}]	[g$_{-PP}$ mmol$_{-Ti}^{-1}$ h^{-1}]
A	4300	1900	n.d.	n.d.
B	4800	1800	n.d.	n.d.
C	840	800	420	400
D	880	1500	600	1000
E	1100	1800	2100	3300
F	820	1500	2300	4200

[a] No polymer was obtained when **A** or **B** was used as the catalyst.

3.3. Formation of Nanostructure Along the Synthetic Steps

3.3.1. PXRD

The solid samples extracted in the course of catalyst preparation (**A** to **F**), as well as the $Mg(OEt)_2$ starting material, were subjected to X-ray total scattering measurements. The X-ray diffraction patterns are shown in Figure 2. The pattern of $Mg(OEt)_2$ exhibits two strong peaks at 2θ = 9 and 11°. The structure of $Mg(OEt)_2$ has not been clearly identified yet, but it is believed that it resembles that of $Mg(OH)_2$ (Brucite, $P\bar{3}m1$), where the H atoms are substituted with ethyl groups, and the split peaks correspond to (001) reflection.[27, 49, 50] That is, the O-Mg-O layers are stacked across a layer of $-C_2H_5$ groups, and hence the peaks at 2θ = 9 and 11° are most likely originated from the stacking of the O-Mg-O layers. A broad peak centered at 2θ = 10° is also observed in the pattern of **A** (right after the first $TiCl_4$ addition), which suggests that the structure of **A** memorizes the layered structure of $Mg(OEt)_2$ to some extent. The same pattern, however, also contains weak reflections at 2θ = 27–40° and 50°, which correspond to the (012)/(104) and (110) reflections of $MgCl_2$, and indicate that the $MgCl_2$ seeds are already formed at the very initial stage of the synthesis. The peak at 2θ = 10° becomes weaker when the temperature is increased up to 60 °C (**B**), and eventually disappears after the addition of DBP and heating up to 110 °C (**C**). Instead, the peak corresponding to the Cl-Mg-Cl stacking along the *c*-axis emerges at 15°. In the following steps of the preparation (from **D** to **F**), the broad peak in the 27–40° range becomes stronger, reflecting the growth of the $MgCl_2$ crystallites both in the lateral and vertical directions. The patterns of **C**–**F** are typical for δ-$MgCl_2$: three broad peaks are observed at around 15°, 27–40°, and 50°, which correspond to (003), (012)/(104), and (110) reflections. The broadness of the peaks indicates the nano size of $MgCl_2$ in all the dimensions, while the merge of the (012) and (104) reflections into a single broad peak (in particular for **C**) dictates the total lack of periodicity in the stacking of Cl-Mg-Cl layers.[8] Hence, PXRD measurements clearly indicate that the $MgCl_2$ crystallites or their

seeds are formed just after the first $TiCl_4$ addition, and they gradually grew through the subsequent steps of preparation, maintaining a disordered structure along the Cl-Mg-Cl stacking direction.

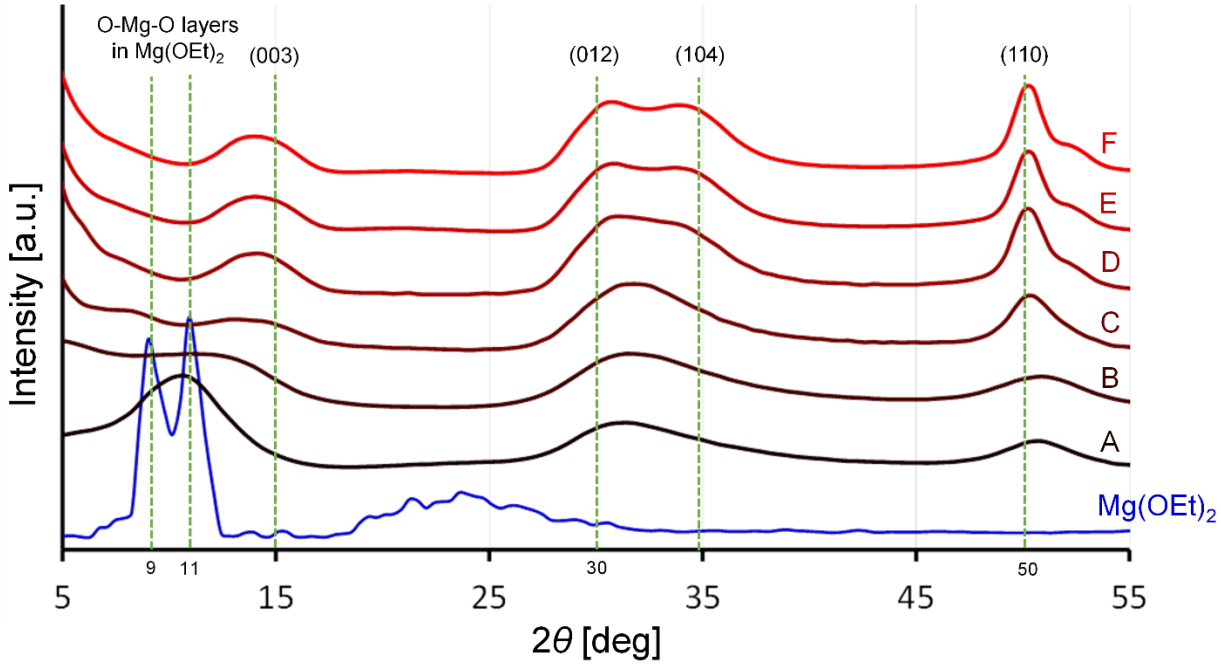

Figure 2. Powder X-ray diffraction (PXRD) patterns of the samples extracted at different steps of the synthesis and of the $Mg(OEt)_2$ starting material. The X-axis was scaled with the wavelength of Cu Kα (λ=1.5418 Å) for comparison with the literature. The typical diffraction peaks of α-$MgCl_2$ are denoted by dotted lines. The patterns are vertically shifted for clarity.

The SEM images of the catalyst samples are shown in Figure S2. The spherical $Mg(OEt)_2$ is an aggregate of plate-like particles with a length of several micrometers.[51] The surface of **A**, just after contact with $TiCl_4$, is notably rough since the plate-like particles partially retain their shape. In **B**, the macroparticles became smoother and more spherical due to the fusion of plate-like particles. After adding the donor (**C**), the surface became even smoother, and the plate-like particles were completely fused. From **C** to **F**, no significant changes were observed. In

addition, the macroparticles seem to grow slightly from **A** to **C**, which is probably due to the fusion of small $Mg(OEt)_2$ macroparticles or the growth of the catalyst primary particles. Such ripening phenomenon has been reported previously, where the resultant catalyst particles were about 10% bigger in diameter than the original $Mg(OEt)_2$ particles.[44, 52]

3.3.2. PDF

The total scattering data were converted into PDFs. Figure 3 shows PDFs of the extracted samples (**A**–**F**) as well as of $Mg(OEt)_2$ and α-$MgCl_2$ in the long-range (part a) and short-range (part b) regions. PDFs directly correlate with the atomic configuration in the real space: i) peak positions correspond to atomic distances; ii) the broadness represents their distribution, including the thermal vibration effect; iii) the relative abundance of the atomic pairs can be estimated by the intensity of the peaks; therefore, the distance at which the amplitude becomes completely negligible corresponds to the crystalline dimensions.[53] For $Mg(OEt)_2$, a weak oscillation can be observed from around 0.5 to 6 nm; however, this is not due to the local atomic configuration, but to density fluctuation originated from a nanostructure, that is most plausibly caused by O-Mg-O layers.[54] The fact that limiting the Q_{min} to 1.0 $Å^{-1}$ completely diminishes the fluctuation also supports this hypothesis (Figure S3). From **A** to **F**, the distance at which the amplitude disappears gradually increases (as marked in yellow in Figure 3a), from r = ca. 2 nm (**A**,**B**) to ca. 4-5 nm (**C**) and to ca. 5.5-6.5 nm (**D**,**F**), suggesting that the $MgCl_2$ crystallites slowly grow during the synthesis.

In the shorter region (Figure 3b), the pattern of $Mg(OEt)_2$ shows a prominent peak at 0.20 nm, which is attributed to the Mg-O atomic pair. For comparison, the distance between Mg and O in $Mg(OH)_2$ is estimated at a very close value, ca. 0.21 nm. The PDF pattern of **A** does not exhibit such peak, providing evidence that the Mg-O bond is immediately converted to Mg-Cl by contacting $Mg(OEt)_2$ with $TiCl_4$. Although there is no traceable Mg-O in the PDF, there is

362 a remnant of the periodic structure formed by $Mg(OEt)_2$ in the PXRD. Such a memory of the
363 precursor structure on PXRD has also been reported in the formation of δ-$MgCl_2$ from
364 $MgCl_2$/Lewis base adducts.[55, 56] The positions of the most relevant peaks in the patterns of the
365 extracted samples are similar to those of α-$MgCl_2$, for example, the peaks at 0.25, 0.35, 0.58,
366 0.63, and 0.97 nm. This fact indicates that the local structures of the extracted samples were
367 almost identical to that of the α-$MgCl_2$ even at the stage of seeds formation (**A**). The relatively
368 weak peak intensity of **A** and **B** over r = 0.5–1.0 nm is due to its finite crystal dimension (<2
369 nm).
370
371

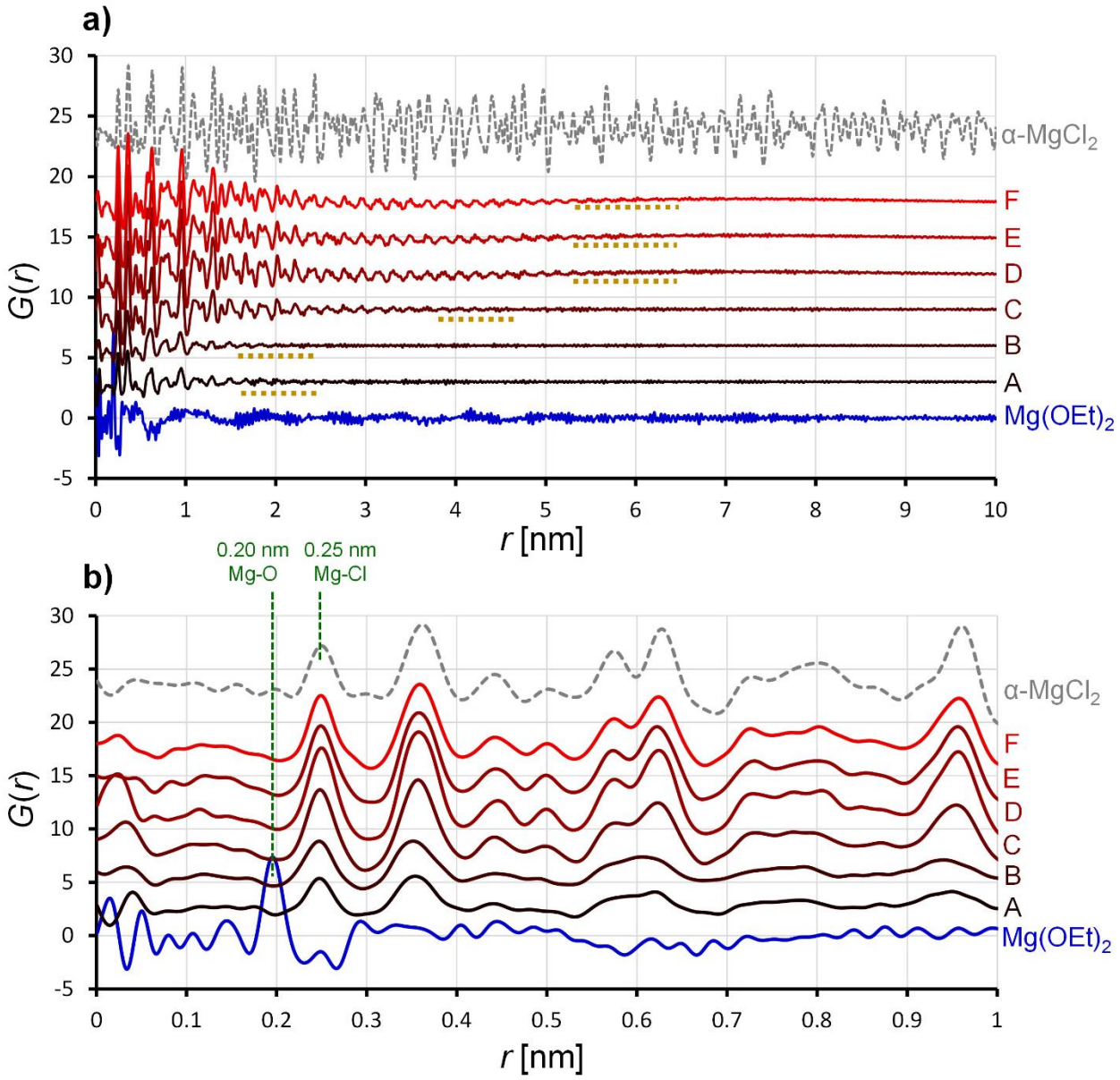

372

373 **Figure 3.** Part a) Atomic pair distribution functions (PDFs) of the extracted samples in the
374 long-range region. Part b) Those in the short-range (part b) region. Q_{min} was set as 0.1 $Å^{-1}$. The
375 PDFs of $Mg(OEt)_2$ and highly crystalline α-$MgCl_2$ (acquired at AichiSR, Q_{max}=15 $Å^{-1}$. See
376 ref[30]) are also provided for comparison purpose. The patterns are vertically shifted for clarity.

377

378 **3.3.3. Quantitative Structural Determination**

379 The structure of δ-$MgCl_2$ in the extracted samples was quantitatively determined by PXRD
380 fitting and cross-validated by PDF fitting, following the same approach discussed in our

previous work.[30] Table 3 summarizes the structural parameters of $MgCl_2$ nanoparticle models as determined by PXRD fitting, where L_a=L_b correspond to the lateral size in the *ab* plane, L_c is the crystallite dimension in the basal direction, and P_c is the probability of finding α-$MgCl_2$ sequences as an indicator of the amount of stacking disorders ranging from 25 to 100%; the accuracy of the fit is also provided in terms of R_w, defined as the residual between the experimental and the simulated patterns. A typical fitting pattern is shown in Figure S4a.

In **A**, obtained just after contacting $Mg(OEt)_2$ with $TiCl_4$, the $MgCl_2$ seeds have a lateral dimension of 1.8 nm and a vertical dimension of 0.3 nm, corresponding to a single Cl-Mg-Cl layer. Heating up to 60 °C (**B**) brings no significant change in the structure of $MgCl_2$ seeds. The addition of donor and heating up to 110 °C (**C**) significantly promotes the growth of the $MgCl_2$ seeds both in the lateral and vertical directions (4.0 nm and 1.4 nm, respectively). Further heating for 2 hours (**D**) induces further growth in the lateral direction (from 4.0 nm to 5.5 nm) as well as a decrease in the stacking disorder (P_c increases from 25% to 40%). The second $TiCl_4$ addition and further aging (**E**,**F**) do not cause a significant structural change, which is consistent with the fact that the amount of Ti and phthalate on $MgCl_2$ is almost kept constant from **D** to **F** (Table 1). It is likely that the presence of DBP (only in the first $TiCl_4$ treatment) is a primary factor to promote the growth of $MgCl_2$.

The obtained $MgCl_2$ nanoparticle models were cross-validated using PDF fitting. Simulated patterns and fitting parameters therein are shown in Figure S4b and Table S2. All the PDF patterns are reasonably fitted with the PXRD-determined nanoparticle models. The fitting accuracy for **A** and **B** was relatively poor ($R_{w,PDF}$ = 0.374 and 0.377), which is likely attributed to the relatively low periodicity (i.e. weaker signals).

Table 3. $MgCl_2$ nanoparticle models derived via PXRD fitting and cross-validated by PDF fitting with the aid of software, DISCUS,[57] PDFgui,[58] and DShaper.[59] L_a = L_b: lateral size in *ab*

406 plane; L_c: crystallite dimension in the basal direction; P_c: indicator of stacking disorder; R_w:
407 indicator of the fitting accuracy.

Sample Name	$L_a = L_b$ [nm]	L_c [nm]	P_c [%]	$R_{w,PXRD}$	$R_{w,PDF}$
A	1.8	0.3	n.a.[a]	0.162	0.374
B	1.8	0.3	n.a.[a]	0.106	0.377
C	4.0	1.4	25	0.151	0.318
D	5.5	1.4	40	0.115	0.278
E	5.8	1.4	46	0.165	0.270
F	6.1	1.4	49	0.143	0.221

408 [a] P_c was not specified as the particle model is composed of a single Cl-Mg-Cl layer.

409

410 **3.4. Morphology of $MgCl_2$ Nanoparticles Along the Synthetic Steps**

411 Far-IR spectroscopy has been applied to all the extracted samples to retrieve information on
412 the morphology of the $MgCl_2$ nanoparticles. As a matter of fact, we have previously
413 demonstrated that the vibrations in the region of 600 – 100 cm^{-1}, which are due to both intra-
414 layer displacement of the atoms in the *ab* plane and inter-layer displacement along *c* axis, are
415 sensitive to the relative extension of the different $MgCl_2$ surfaces.[43] Moreover, vibrations
416 involving Ti-Cl, Ti-O and Mg-O also fall in this spectral range, so that Far-IR can provide
417 information also on the adsorbates at $MgCl_2$ surfaces, including the Ti species.

418 Figure 4 displays the evolution of the Far-IR spectra along the synthetic steps, together with
419 the spectrum of the $Mg(OEt)_2$ starting material.

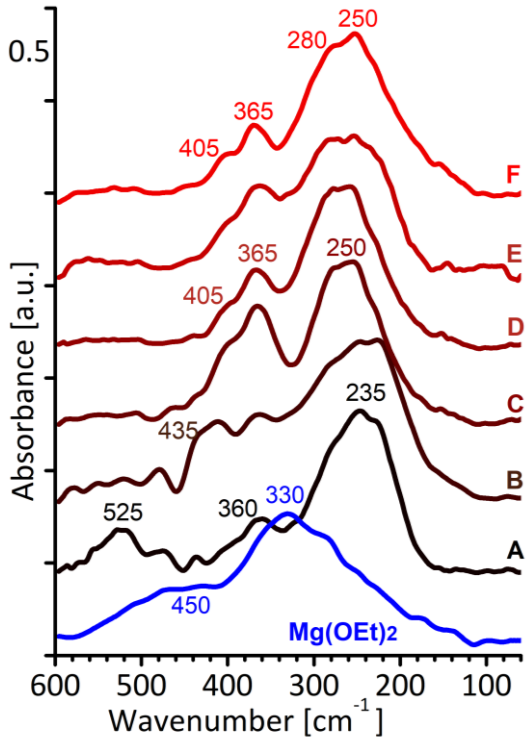

Figure 4. Far-IR spectra of the extracted samples and of the $Mg(OEt)_2$ precursor. The spectra are vertically stacked for clarity.

The Far-IR spectrum of $Mg(OEt)_2$ is characterized by two main absorptions centered at 330 and 450 cm^{-1}, very broad and overlapping to each other. Similar bands have been already observed in the past for different $MgCl_2$ adducts with alcoholates and alkoxides, and assigned to the vibrations of Mg-O bonds.[60-62] As observed in the PDF analysis for the same sample, these bands are no more observed already at the first step of the synthesis, while they are replaced by the vibrational modes characteristic of $MgCl_2$. The spectrum of **A** shows a main absorption band centered at 235 cm^{-1}, together with two weaker bands at 525 and 360 cm^{-1}. The sharp band at 235 cm^{-1} is assigned to the basal (001) surface,[43] in well agreement with the PXRD analysis according to which the first $MgCl_2$ seeds are mostly formed as monolayers. The band at 525 cm^{-1}, instead, is attributed to the ν(Ti-O) vibrations of 4-fold coordinated $Ti(OEt)_xCl_{4-x}$ species (vide infra).[63] The relatively high intensity of this band is in well

agreement with the high and nearly equimolar Ti and OEt percentages in **A** (2.42 and 2.09 mmol g^{-1}, respectively). Finally, the band at 360 cm^{-1} is attributed to a few ethoxide residues on the $MgCl_2$ seeds.

In the spectrum of **B**, the main absorption band is still located at 235 cm^{-1}, indicating that even after heating at 60 °C $MgCl_2$ particles mainly expose the basal surface (001). The band at 525 cm^{-1} is no more observed, while a new band with similar intensity is present at 435 cm^{-1}. This band is assigned to ν(Ti-Cl) of 6-fold coordinated Ti species,[11] and indicates that a fraction of the Ti ethoxy chloride complexes are chemisorbed on the $MgCl_2$ seeds during the warm-up process up to 60 °C. Unfortunately, the destiny of this band in the following steps of the synthesis cannot be further investigated because of the drastic decrease of the Ti loading (to 0.56 mmol g^{-1} in **F**), which makes the band too weak in intensity.

The addition of DBP (**C**) causes a significant change in the Far-IR spectrum: the main absorption band upward shifts to 250 cm^{-1} (with a shoulder at 280 cm^{-1}) and a sharp and intense band appears at 365 cm^{-1} (with a pronounced hump at 405 cm^{-1}). According to previous calculations, both manifestations can be associated to a morphological reconstruction of the $MgCl_2$ crystallites, which now do not expose anymore exclusively the basal (001) surface. In particular, the (110) surface is the principal responsible for the main signals at 250 and 365 cm^{-1}, while both the (012) and (015) surfaces significantly contribute at 280 and 405 cm^{-1}.[43]

From **D** on, all the Far-IR spectra are similar to each other and to the spectrum of the final ZN catalyst (**F**). The features of the spectra are the same as already discussed in our previous work.[43] Briefly, with respect to the spectrum of **C**, the main absorption band at 250 cm^{-1} undergoes a slight enlargement and the band at 365 cm^{-1} slightly decreases in intensity. Overall, the spectrum indicates that $MgCl_2$ nanoparticles expose a large variety of surfaces, among which the relatively most abundant is the (110) one. It is worth noticing that such a surface has been claimed to be one of the most catalytically relevant ones.[64-67]

3.5. Surface Species Along the Synthetic Steps

The evolution of the surface species during ZN catalyst synthesis was investigated by IR spectroscopy in the Mid-IR region, as reported in Figure 5a. The spectrum of $Mg(OEt)_2$ is analogous to the spectra of Mg alkoxides already reported and described in literature.[68, 69] Briefly, most of the bands are due to the vibrational modes of the OEt moieties: the $\nu(CH_x)$ bands at 2800-3000 cm^{-1}, the $\delta(CH_2)$ and $\delta(CH_3)$ bands at 1450 and 1380 cm^{-1}, ν(C-O) at 1120 cm^{-1}, ν(C-C) at 1050 cm^{-1} and some rocking modes at 890 cm^{-1}. Below 600 cm^{-1} the tail of the absorption band due to the ν(Mg-O) vibrations, contributing in the Far-IR region, is also observed.

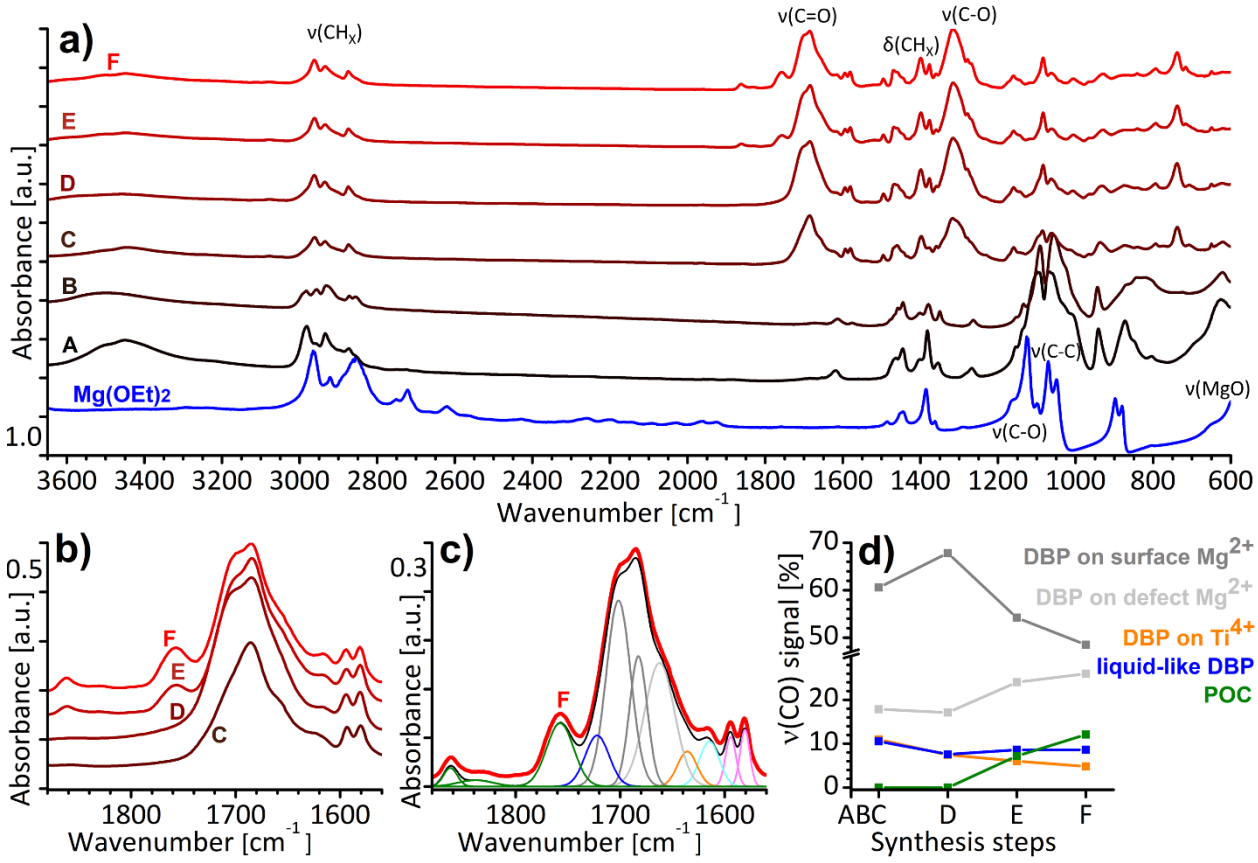

Figure 5. Part a) IR spectra of the extracted samples, normalized to the optical thickness of the pellets. Part b) Magnification of the **C**-**F** spectra in the ν(C=O) region. Part c) Curve fitting in the ν(C=O) region for **F** (the black curve is the sum of all the calculated contributions). Part d)

Evolution of individual ν(C=O) components along the synthetic steps. The components are liquid-like physisorbed DBP, DBP on $MgCl_2$ surfaces, DBP on defective Mg^{2+} sites, DBP on Ti^{4+}, and POC.

The original bands due to the Mg-ethoxide groups are no more observable in the spectrum of **A**. Nevertheless, the spectrum still contains intense bands in the ν(CH_x), δ(CH_x), ν(C-O) and ν(C-C) regions, which correspond well to those observed in the spectra of tetrahedral $Ti(OEt)_2Cl_2$ and $Ti(OEt)_3Cl$ complexes.[63] Hence, at this stage most of the ethoxide groups look associated into $TiCl_x(OEt)_{4-x}$ species rather than incompletely chlorinated $Mg(OEt)_xCl_{2-x}$. Beside the ethoxide bands, the spectrum of **A** displays a weak and broad band in the ν(OH) region (around 3400 cm^{-1}), which is due to a small amount of moisture contamination. The spectrum of **B**, obtained after heating **A** up to 60 °C, shows only small changes in the position of the bands ascribed to the ethoxide species, which are compatible with the chemisorption of the Ti ethoxide chloride complexes and a change in the coordination of the Ti cations from tetrahedral to octahedral.

The IR spectra radically change after the addition of DBP in the reaction mixture (**C**).[70] Most of the bands associated to the ethoxide groups drastically decrease in intensity after the addition of DBP (**C**), indicating that the ethoxide groups are mostly removed, in perfect agreement with the chemical composition of the sample in Table 1. The spectra of **C** to **F** are all dominated by the vibrational features of DBP, with the characteristic ν(C=O) band around 1700 cm^{-1} (as magnified in Figure 5b). The analysis of the ν(C=O) region allows to obtain information on the coordination modes of DBP at the $MgCl_2$ surfaces and hence, indirectly, on the types of exposed sites. A curve fitting of the ν(C=O) region has been performed for the spectra of **C**-**F**, as frequently reported in the literature, where each computed band has been assigned on the basis of the literature. By way of example, Figure 5c displays the curve fitting of the spectrum

of the final catalyst (**F**), which includes all the possible ν(C=O) contributions: for liquid-like DBP at 1728 cm^{-1},[71, 72] DBP in interaction with different Mg^{2+} sites at 1657, 1680 and 1707 cm^{-1},[71-74] DBP in interaction with $TiCl_4$ at 1634 cm^{-1},[75, 76] and the POC produced by a side reaction between DBP and $TiCl_4$ at 110 °C[42] at 1758, 1836 and 1862 cm^{-1} (identical bands were observed by directly co-milling $MgCl_2$ and POC).[76, 77] The fit is completed by including the two ring vibrations of the ortho-disubstituted phenyl ring at 1581 and 1595 cm^{-1},[78] and an additional band at 1615 cm^{-1} ascribable to δ(OH) of water traces. Focusing on the three bands due to DBP in interaction with different Mg^{2+} sites, the band at 1707 cm^{-1} can be assigned to DBP both in a chelate configuration on 4-fold coordinated Mg^{2+} sites (the most thermodynamically favored configuration for DBP on the (110) surface) and monodentate on 5-fold coordinated Mg^{2+} sites,[79, 80] the band at 1680 cm^{-1} is ascribed to monodentate DBP at 4-fold coordinated Mg^{2+} sites,[79, 80] whereas the band at 1657 cm^{-1} is due to DBP on defect sites.[71, 73, 74] It is important to notice that, at a difference than what happens with ethylbenzoate, it is not possible to quantify the DBP coordinated at 4-fold and 5-fold Mg^{2+} sites, but only to discriminate between DBP adsorbed at $MgCl_2$ surfaces and defects.

By estimating the integrated areas of each ν(C=O) band in the series of spectra for **C**-**F**, it has been possible to estimate in a semi-quantitative way the relative abundances of each species at the different synthesis steps, as reported in Figure 5d.[81] A few conclusions can be drawn as follows.

i. As soon as DBP is added (**C**), some DBP molecules are trapped as liquid-like in the interparticle pores of the material (blue line). This is compatible with the porosity data reported by Chumachenko et al.[42] The amount of liquid DBP slightly decreases in the following steps.

ii. Moreover, as soon as DBP is added to the reaction mixture (**C**), a non-negligible amount of a complex with $TiCl_4$ (orange line) is formed at $MgCl_2$ surfaces. The

thermodynamics driving this process was evaluated in the past by experimental calorimetric measurements[82] and by theoretical calculations.[83] An analogous behavior has been already observed upon dosing ethyl benzoate (EB) on $MgCl_2/TiCl_4$ from the vapor phase.[84] According to the trend in Figure 5d, some of these complexes are washed away during the successive steps of the catalyst synthesis, but not all of them.

iii. DBP on $MgCl_2$ surfaces (grey line) are the most abundant species in all the samples, although their amounts slightly decrease along the series in favor of DBP on defective sites (light grey line), likely because their formation and stabilization is promoted by DBP itself.[85]

iv. Finally, after the second addition of $TiCl_4$ (**E**), some DBP molecules are converted into phtaloyl chloride,[42] which was not present at all upon the first addition of $TiCl_4$. This process increases over time upon aging the sample at 110 °C in the reaction mixture (**F**).

3.5. Local Structure of the Ti Centers Along the Synthetic Steps

Finally, DR UV-Vis spectroscopy has been applied to monitor the evolution of the Ti species from an electronic point of view during the ZN catalyst synthesis (Figure 6). Even though the oxidation state remains the same (+4), the DR UV-Vis spectra change along the series, reflecting changes in the titanium coordination sphere.

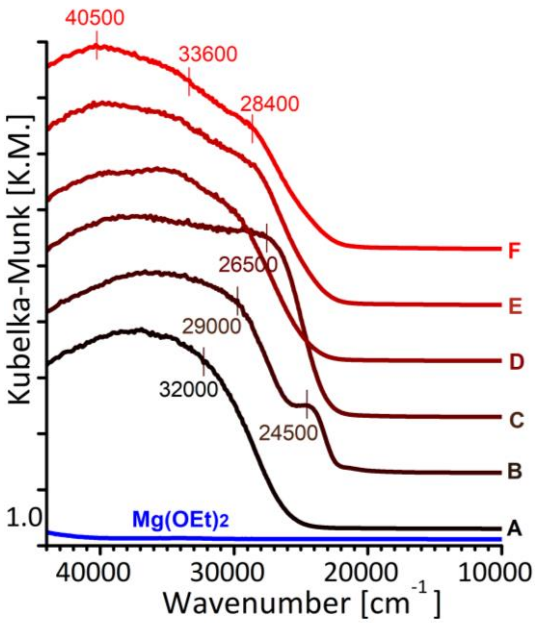

543

544 **Figure 6.** DR UV-Vis spectra of the extracted samples and of the $Mg(OEt)_2$ precursor. The
545 spectra are vertically stacked for clarity.

546 Whereas the spectrum of $Mg(OEt)_2$ displays no absorption in the whole UV-Vis region, the
547 spectra of the extracted samples are dominated by intense absorptions above 30000 cm^{-1}, due
548 to several charge transfer (CT) transitions involving the Ti metal centers and their ligands.
549 Since many contributions overlap to each other at high energy and hence cannot be clearly
550 identified, the analysis will focus on the absorption band at lower energy, which is more easily
551 identifiable and straightforwardly assigned to a $Cl(\pi) \rightarrow Ti(d)$ CT transition.[86, 87] Moreover, on
552 this band the Jorgensen semi-empirical rule on the optical electronegativity of transition metals
553 and their ligands can be applied.[88]

554 The spectrum of **A** shows the maximum of the first absorption at ca. 32000 cm^{-1}, which is
555 compatible with a charge transfer transition from Cl^- ligands to a 4-fold coordinated Ti^{4+}
556 (expected around 34500 cm^{-1} according to the Jorgensen rule).[88] This indicates that most of the
557 Ti in **A** is present as physisorbed 4-fold coordinated $TiCl_x(EtO)_{4-x}$ species,[63] in fair agreement
558 with both Far-IR and Mid-IR data, and compatibly with the sequence proposed by Brambilla
559 et al. for $TiCl_4$ chemisorption on $MgCl_2$.[12] Then, after heating at 60 °C (**B**), the main absorption

560 downward shifts to ca. 29000 cm^{-1} and a new sharp band appears at 24500 cm^{-1}. The downward
561 shift of these bands is associated to a change in the coordination of the Ti ions from 4-fold to
562 6-fold (the theoretical value for the CT transition from Cl^- ligands to octahedral Ti^{4+} is 28200
563 cm^{-1}),[88] indicating that 4-fold coordinated $TiCl_x(EtO)_{4-x}$ species at 60 °C have adjusted in the
564 more stable 6-fold coordinated octahedral configuration on the nascent $MgCl_2$ surfaces. This
565 is again in agreement with the analysis of the Far-IR and Mid-IR spectra. Notably, an analogous
566 trend was observed during $TiCl_4$ chemisorption from the vapor phase onto bare $MgCl_2$.[89] The
567 two bands, which differ of ca. 4500 cm^{-1}, might arise from the same Cl(π)→Ti(d) CT transition
568 localized on slightly different Ti species (for example with a different number of ethoxide
569 ligands) and/or from two Cl(π)→Ti(d) CT transitions on the same Ti cation from two different
570 Cl species (e.g. axial and equatorial Cl atoms with respect to the ethoxide ligands).[90]
571 The successive synthetic step (**C**) is dominated by the introduction of DBP, which not only
572 coordinates to the $MgCl_2$ surfaces and defects, but also directly to the Ti centers, as revealed
573 by the IR spectra in Figure 5c. The corresponding UV-Vis spectrum shows an intense band
574 peaked at 26500 cm^{-1}, which is always ascribed to a Cl(π)→Ti(d) CT transition for 6-fold
575 coordinated Ti sites, but with a slightly different environment than before. Indeed, IR
576 spectroscopy revealed that, at this step, most of the ethoxide ligands have been removed, and
577 $TiCl_4$-DBP complexes are formed. Most of the $TiCl_4$-DBP complexes are then removed from
578 $MgCl_2$ surfaces in the following steps of ZN catalyst synthesis because of the several washes
579 with toluene, and that absorption band is almost no more present in the following spectra.
580 Therefore, spectra of **D**, **E**, and **F** are all dominated by the absorption bands typical of
581 Cl(π)→Ti(d) CT transitions for Ti^{4+} in a 6-fold coordination, with small differences due to
582 slight distortions in the geometry and minor changes in the effective charge distribution.[86]
583
584 **3.6. Evolution of the samples upon TEAl activation**

TEAl activation has been investigated with an Al:Ti ratio of 2:1, in order to simulate the excess of activator used in the polymerization tests in Section 3.2. Figure 7 displays some significant results obtained by DR UV-Vis and IR spectroscopies.

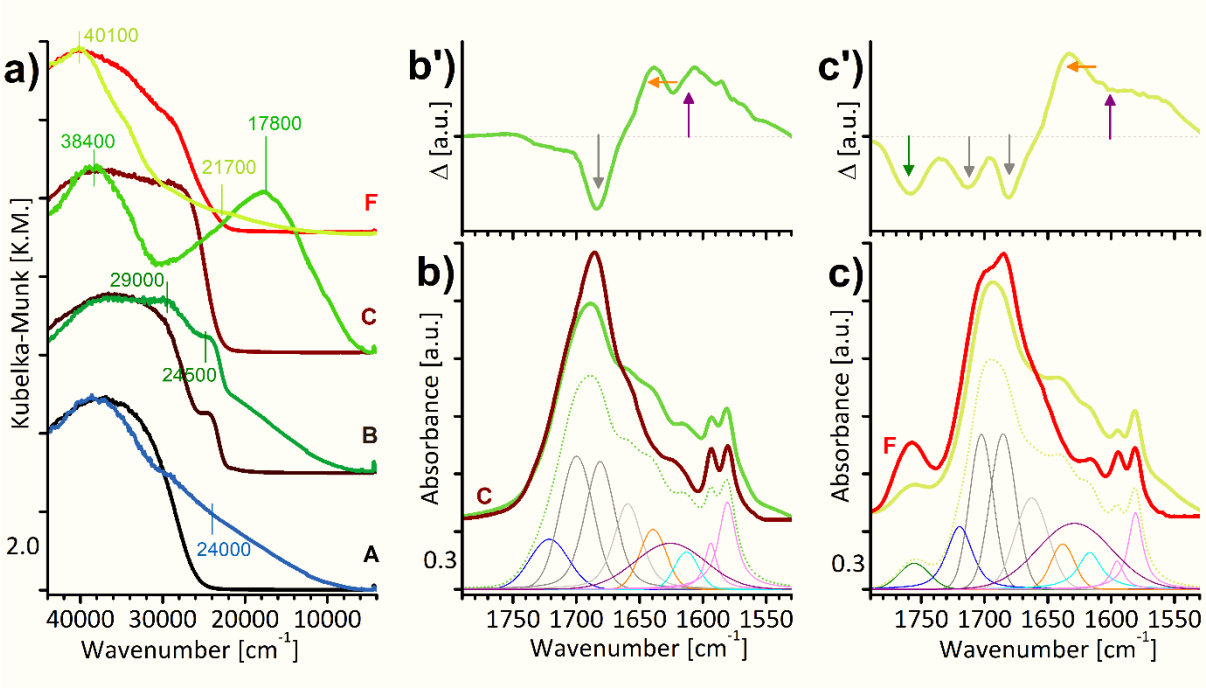

Figure 7. Part a) DR UV-Vis spectra of samples **A**, **B**, **C** and **F**, before and after TEAl activation. Part b) Magnification in the ν(C=O) of the IR spectra of **C** before and after TEAl activation. Curve fitting is also shown for activated **C**. Part b') Difference spectrum calculated by subtracting to the spectrum of activated **C** the spectrum before TEAl activation. Parts c and c') same as in parts b and b' for **F**.

In the UV-Vis spectrum of **A**, the position of the main absorption (that was assigned to a Cl(π)→Ti(d) CT transition) upward shifts at 38400 cm^{-1}, which is compatible with the reduction of the Ti sites from +4 to +3 oxidation state.[88] At the same time, a broad absorption grows up centered at about 24000 cm^{-1}, whose position corresponds to a Ti^{3+} d-d transition, but whose intensity is much higher. Similar bands have been already observed in the past for TEAl-

601 activated ZN catalysts and assigned to intersite d-d transition involving two Ti^{3+} sites bridged
602 by a Cl^- ligand, thus assuming a partial charge transfer character;[91] for this reason, they have
603 been considered as proof of the formation of $TiCl_3$ clusters. In **A**, the formation of $TiCl_3$ clusters
604 is favored by the high mobility of physisorbed $TiCl_x(OEt)_{4-x}$ species.
605 An analogous trend is observed also in **B**, although in this case the two bands at 29000 and
606 24500 cm^{-1} remain unaltered, revealing that the fraction of 6-fold coordinated $TiCl_x(EtO)_{4-x}$
607 species responsible for those bands are evidently less reactive towards TEAl.
608 The spectrum of activated **C** is characterized by two very intense and well-defined absorption
609 bands at 38400 and 17800 cm^{-1}. The former is assigned to a Cl(π)$\rightarrow$Ti(d) CT transition for a
610 Ti in the +3 oxidation state (as already discussed for **A**), while the latter is very peculiar, quite
611 different from the fingerprint of the $TiCl_3$ clusters typically observed in TEAl-activated ZN
612 catalysts. Instead, that band recalls the UV-Vis spectrum reported in the literature for a
613 $[TiCl_4(thf)_2]_1[MgCl_2(thf)_{1.5}]_2$ adduct after reaction with an Al-alkyl (trioctyl-aluminum, in that
614 case).[90] Therefore we can imagine the formation of DBP-bonded $TiCl_3$.
615 Finally, the DR UV-Vis spectrum of activated **F** is characterized by the almost complete
616 erosion of the bands at 33600 and 28400 cm^{-1} that were present before the reaction with TEAl,
617 leaving the place for an intense CT transition absorption band at 40100 cm^{-1} and a quite weak
618 band at 21700 cm^{-1}, which is attributed to isolated, 5-fold coordinated and alkylated Ti^{3+}
619 species (although the broadness of the band reveals a certain heterogeneity of the sites, in terms
620 of slightly different structural parameters and chemical surroundings).[92] According to the data
621 of polymerization activity shown in Figure 1, those species are thus the main responsible for
622 propylene polymerization.
623 On the contrary, IR spectroscopy provides new insights on the fate of the donor after TEAl
624 activation, which is one of main open questions in ZN catalysis. As a matter of fact, depending
625 on the temperature a more or less large fraction of DBP is known to be cleaned up by TEAl (a

minimal fraction at room temperature, almost the totality at about 100 °C),[93] but the state of the molecules remaining on the catalyst surfaces is still unclear. Figure 7b and **Figure 7**c display the magnification of the ν(C=O) region for **C** and **F** before and after TEAl activation at room temperature, revealing an analogous trend for the samples corresponding to the initial DBP addition and to the sample at the end of the synthesis (the quantification of the integrated areas for all the individual ν(C=O) components are reported in Table S3).

The fraction of liquid-like DBP is roughly constant, indicating that DBP molecules trapped within the pores during ZN catalyst synthesis are not washable and not accessible even for TEAl. The fraction of DBP adsorbed on Mg^{2+} sites drops down (especially for surface Mg^{2+} sites), together with the fraction of POC in **F**, in the face of the appearance of a new component at ca. 1625 cm^{-1}, which can be reasonably assigned to DBP in interaction with the Al^{3+} centers, coming from both the TEAl molecules in excess and the $AlCl_xEt_{3-x}$ by-products adsorbed on the catalyst. Finally, the fraction of DBP in interaction with the Ti centers is almost constant, but the position of the band shifts at higher frequencies (from 1634 to 1640 cm^{-1}), likely because of the reduction from Ti^{4+} to Ti^{3+}. This suggests that the $TiCl_4$-DBP complexes that are formed on the catalyst surface and remain after the following thermal and chemical treatments, they do remain even after TEAl activation and are actually activated, so that a possible role in the overall catalytic process cannot be discarded.

4. Conclusions

The multi-technique investigation presented in this work sheds light on the chemical reactions and structural evolution taking place during the formation of an industrial-like Ziegler-Natta pre-catalyst, starting from the $Mg(OEt)_2$ precursor and in the presence of DBP as an internal donor. Five intermediate samples have been extracted from the glass reactor at different stages, plus the final catalyst, and analyzed in terms of structure, morphology, and

surface species. All the techniques converge in demonstrating that as soon as $Mg(OEt)_2$ is contacted with $TiCl_4$, all Mg-O bonds are converted into Mg-Cl ones, forming the first seeds of $MgCl_2$, which appear as Cl-Mg-Cl monolayers with a lateral dimension of below 2 nm, and releasing $TiCl_x(OEt)_{4-x}$ as by-products (first physisorbed as 4-fold coordinated, and then chemisorbed as 6-fold coordinated). Those species efficiently polymerize ethylene but not propylene.

The addition of the DBP electron donor significantly promotes the growth of $MgCl_2$ seeds with the preferential exposure of lateral surfaces, including those relevant for the catalysis; as a matter of fact, only after the DBP addition the catalyst becomes active in propylene polymerization. Most of DBP is coordinated to $MgCl_2$ surfaces, corroborating the hypothesis that the influence of the electron donors on the stereoselectivity of ZN catalysts is mostly due to a steric modulation of the Ti surroundings. However, a non-negligible fraction of DBP is actually complexed to the Ti ions, and some of these species remain in ZN catalyst even at the end of the synthesis and can be effectively activated by TEAl (at least at room temperature, further investigation will be needed to monitor the activation process at higher temperatures).

Finally, the second addition of $TiCl_4$ is mostly chemisorbed as 6-fold coordinated on $MgCl_2$ surface largely replacing the $TiCl_x(OEt)_{4-x}$ species, although a fraction of $TiCl_4$ is also consumed in a side reaction with DBP, as testified by the formation of phthaloyl chlorides. The newly formed Ti species are remarkably more active in propylene polymerization (the production of polypropylene per hour per Ti mole almost triples at this step). It is worth noticing that the aging at 110 °C allows a further rearrangement of the species in the material (both in $MgCl_2$ morphology, and in DBP disposition, and in the local structure of the Ti sites), further increasing the activity towards propylene polymerization, which is attributed to isolated, 5-fold coordinated and alkylated Ti^{3+} species. This demonstrates the positive effect of

the final thermal treatment to afford truly performant ZN catalysts. All these findings are schematically summarized in Figure 8.

More in general, this unprecedented knowledge of all the chemical reactions and structural evolution at each step of ZN catalyst synthesis will drive the choices of the researchers from both academia and companies that aim at the optimization of this complex multicomponent material.

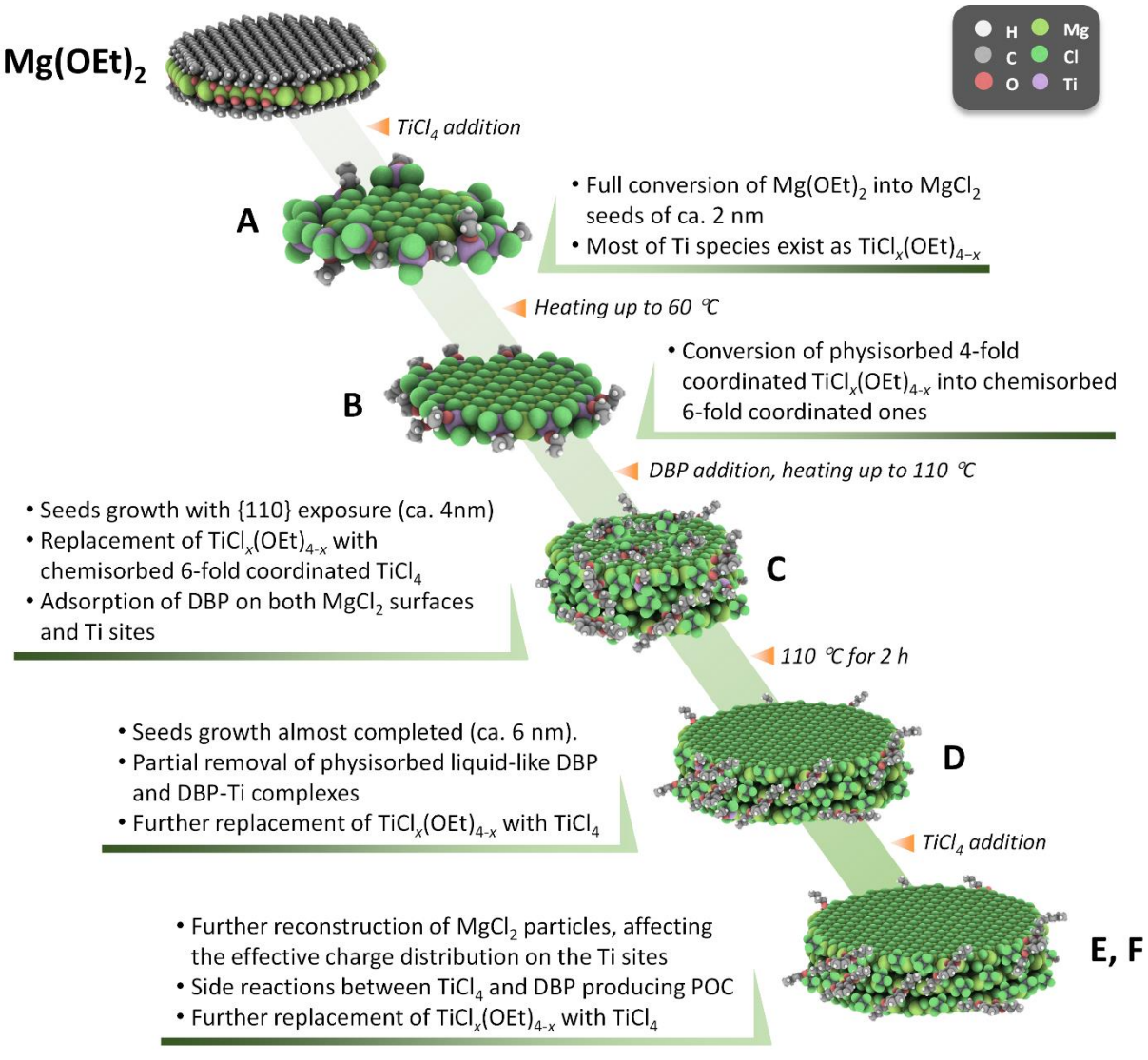

Figure 8. Schematic representation of catalyst formation from $Mg(OEt)_2$. The $MgCl_2$ nanoparticle models were drawn by atomistic system rendering software Speck with the aid of Vesta.[94]

AUTHOR INFORMATION

Corresponding Author

Alessandro Piavano *E-mail: alessandro.piovano@unito.it

Toshiaki Taniike *E-mail: taniike@jaist.ac.jp

Author Contributions

A.P.† and T.W.† wrote the manuscript. A.P.† and A.A. acquired and analyzed the vibrational and electronic spectroscopies. T.W.† performed sample preparation, chemical analysis, and the synchrotron X-ray total scattering experiments. G.T. created some nanoparticle models and helped computational simulation. T.I. acquired SEM observation and interpreted the results. Z.D. performed DSC measurement and analysis. M.T. contributed to finalize the manuscript. P.C. designed and performed the polymerization tests. E.G. and T.T. conceived the concept and supervised the entire research.

†These authors contributed equally.

Funding Sources

DPI project #802

JSPS KAKENHI Grant Number JP20J15042

Notes

The authors declare no competing financial interest.

Supporting Information

The polymer characterization results, the SEM images of the extracted samples (**A**–**F**), the PDFs of the samples where Q_{min} was intentionally increased to 1.0 $Å^{-1}$, typical PXRD and PDF fitting results, the fitting parameters obtained by PDFgui, and the contributions of individual ν(C=O) components for the IR spectra of **C** and **F**, before and after TEAl activation are available. This information is available free of charge on the ACS Publications website.

ACKNOWLEDGMENT

The authors appreciate Japan Polychem Corp. and Tosoh Finechem Corp. for the reagent donation. The authors also appreciate Toho Titanium Co. Ltd. for GPC measurement. The synchrotron X-ray total scattering experiments were performed at BL04B2 in SPring-8 with the approval of RIKEN (Proposal No. 2019A1143 and 2020A1231). The work of A.P., T.W., C.P., E.G., and T.T. forms part of the research programme of DPI, project #802. The work of G.T. was supported by JSPS KAKENHI Grant Number JP20J15042.

REFERENCES

1. Jansz, J., In *Global PO&E News Analysis*, Chemical Market Resources, Inc.: 2015.

2. *Polyolefins Market Share, Size, Trends, Industry Analysis Report By Feedstock (Polyethylene, Polypropylene, Ethylene Vinyl Acetate, Thermoplastic Olefins, Others), By Application (Film & Sheet, Injection Molding, Blow Molding, Extrusion Coating, Fiber, Others), By Regions, Segments & Forecast, 2019 - 2026*. Polaris Market Research: 2019.

730 3. Albizzati, E.; Giannini, U.; Collina, G.; Noristi, L.; Resconi, L., Catalysts and
731 polymerizations. In *Polypropylene Handbook*, Moore, E. P. J., Ed. Hanser-Gardner
732 Publications: Cincinnati (Ohio, USA), 1996.

733 4. Galli, P.; Vecellio, G., Technology: driving force behind innovation and growth of
734 polyolefins. *Prog. Polym. Sci.* **2001,** *26* (8), 1287-1336.

735 5. Vittoria, A.; Meppelder, A.; Friederichs, N.; Busico, V.; Cipullo, R., Demystifying
736 Ziegler-Natta Catalysts: The Origin of Stereoselectivity. *ACS Catal.* **2017,** *7* (7), 4509-4518.

737 6. Gote, R. P.; Mandal, D.; Patel, K.; Chaudhuri, K.; Vinod, C.; Lele, A. K.; Chikkali,
738 S. H., Judicious reduction of supported Ti catalyst enables access to disentangled ultrahigh
739 molecular weight polyethylene. *Macromolecules* **2018,** *51* (12), 4541-4552.

740 7. Delogu, F.; Mulas, G.; Schiffini, L.; Cocco, G., Mechanical work and conversion
741 degree in mechanically induced processes. *Mater. Sci. Eng., A* **2004,** *382* (1), 280-287.

742 8. Galli, P.; Barbé, P. C.; Guidetti, G.; Zannetti, R.; Marigo, A.; Bergozza, M.; Fichera,
743 A., The activation of MgCl2-supported Ziegler-Natta catalysts: A structural investigation. *Eur.*
744 *Polym. Chem.* **1983,** *19*, 19-24.

745 9. Noristi, L.; Barbè, P. C.; Baruzzi, G., Effect of the internal/external donor pair in high-
746 yield catalysts for propylene polymerization, 1. Catalyst-cocatalyst interactions. *Makromol.*
747 *Chem.* **1991,** *192* (5), 1115-1127.

748 10. Soga, K.; Ohgizawa, M.; Shiono, T., Copolymerization of ethylene and propene with
749 a TiCl4/MgCl2-Al(C2H5)3 catalyst system using a stopped-flow method. *Makromol. Chem.*
750 **1993,** *194* (8), 2173-2181.

751 11. Brambilla, L.; Zerbi, G.; Nascetti, S.; Piemontesi, F.; Morini, G., Experimental and
752 Calculated Vibrational Spectra and Structure of Ziegler-Natta Catalyst Precursor: 50/1
753 Comilled MgCl2-TiCl4. *Macromolecular Symposia* **2004,** *213*, 287-301.

754 12. Brambilla, L.; Zerbi, G.; Piemontesi, F.; Nascetti, S.; Morini, G., Structure of MgCl2-
755 TiCl4 complex in co-milled Ziegler-Natta catalyst precursors with different TiCl4 content:
756 Experimental and theoretical vibrational spectra. *Journal of Molecular Catalysis a-Chemical*
757 **2007,** *263* (1-2), 103-111.

758 13. Wada, T.; Thakur, A.; Chammingkwan, P.; Terano, M.; Taniike, T.; Piovano, A.;
759 Groppo, E., Structural Disorder of Mechanically Activated δ-MgCl2 Studied by Synchrotron
760 X-ray Total Scattering and Vibrational Spectroscopy. *Catalysts* **2020,** *10* (9), 1089.

761 14. Chung, J. S.; Song, I. K.; Lee, W. Y.; Park, H. M., Morphology control of a MgCl2-
762 supported Ziegler-Natta catalyst by the recrystallization method. *Macromol. Chem. Phys.*
763 **1995,** *196* (4), 1205-1210.

764 15. Choi, J. H.; Chung, J. S.; Shin, H. W.; Song, I. K.; Lee, W. Y., The effect of alcohol
765 treatment in the preparation of MgCl2 support by a recrystallization method on the catalytic
766 activity and isotactic index for propylene polymerization. *Eur. Polym. J.* **1996,** *32* (4), 405-
767 410.

768 16. Parada, A.; Rajmankina, T.; Chirinos, J., Study of the MgCl2 recrystallization
769 conditions on Ziegler-Natta catalyst properties. *Polym. Bull.* **1999,** *43* (2), 231-238.

770 17. Piyavit, P.; Piyasan, P., Comparison of Activity of Ziegler-Natta Catalysts Prepared by
771 Recrystallization and Chemical Reaction Methods towards Polymerization of Ethylene.
772 *ENGINEERING JOURNAL* **2009,** *13* (1), 57-64.

18. Puhakka, E.; Pakkanen, T. T.; Pakkanen, T. A., Theoretical Investigations on Heterogeneous Ziegler-Natta Catalyst Supports: Stability of the Electron Donors at Different Coordination Sites of MgCl2. *J. Phys. Chem. A* **1997,** *101* (34), 6063-6068.

19. Andoni, A.; Chadwick, J. C.; Niemantsverdriet, H. J. W.; Thune, P. C., A preparation method for well-defined crystallites of Mgcl(2)-supported Ziegler-Natta catalysts and their observation by AFM and SEM. *Macromol. Rapid Commun.* **2007,** *28* (14), 1466-1471.

20. Andoni, A.; Chadwick, J. C.; Niemantsverdriet, H. J. W.; Thune, P. C., The Role of Electron Donors on Lateral Surfaces of MgCl2-Supported Ziegler-Natta Catalysts: Observation by AFM and SEM. *J. Catal.* **2008,** *257* (1), 81-86.

21. Thushara, K. S.; Mathew, R.; Ajithkumar, T. G.; Rajamohanan, P. R.; Bhaduri, S.; Gopinath, C. S., $MgCl_2$-4$(CH_3)_2CHOH$: a new molecular adduct and super active catalyst support. *J. Phys. Chem. Lett.* **2009,** *113*, 8556-8559.

22. Thushara, K. S.; D'Amore, M.; Piovano, A.; Bordiga, S.; Groppo, E., The Influence of Alcohols in Driving the Morphology of Magnesium Chloride Nanocrystals. *ChemCatChem* **2017,** *9* (10), 1782–1787.

23. Nissinen, V. H.; Koshevoy, I. O.; Pakkanen, T. T., Crystalline magnesium chloride-electron donor complexes: new support materials for Ziegler-Natta catalysts. *Dalton Trans.* **2017,** *46* (13), 4452-4460.

24. Taveira Magalhães, D. N.; Do Coutto Filho, O.; Coutinho, F. M. B., Ziegler-Natta catalysts for ethylene and propylene polymerizations supported on the products of thermal desolvation of the adducts of magnesium chloride with methyl and ethyl alcohols. *Eur. Polym. J.* **1991,** *27* (10), 1093-1096.

795 25. Lee, D. H.; Jeong, Y. T.; Soga, K., In situ formation of magnesium chloride support
796 and internal donor during preparation of propylene polymerization catalysts. *Ind. Eng. Chem.*
797 *Res.* **1992,** *31* (12), 2642-2647.

798 26. Dashti, A.; Ramazani Sa, A.; Hiraoka, Y.; Kim, S. Y.; Taniike, T.; Terano, M.,
799 Kinetic and morphological study of a magnesium ethoxide-based Zieglerâ€“Natta catalyst for
800 propylene polymerization. *Polym. Int.* **2009,** *58* (1), 40-45.

801 27. Funako, T.; Chammingkwan, P.; Taniike, T.; Terano, M., Alternation of Pore
802 Architecture of Ziegler-Natta Catalysts through Modification of Magnesium Ethoxide.
803 *Macromol. React. Eng.* **2015,** *9* (4), 325-332.

804 28. Klaue, A.; Kruck, M.; Friederichs, N.; Bertola, F.; Wu, H.; Morbidelli, M., Insight
805 into the Synthesis Process of an Industrial Ziegler-Natta Catalyst. *Ind. Eng. Chem. Res.* **2019,**
806 *58* (2), 886-896.

807 29. Nissinen, V.; Pirinen, S.; Pakkanen, T. T., Unexpected cleavage of ether bonds of 1,3-
808 dimethoxypropane in Grignard-Wurtz synthesis of a MgCl2-donor adduct. *J. Mol. Catal. A:*
809 *Chem.* **2016,** *413*, 94-99.

810 30. Wada, T.; Takasao, G.; Piovano, A.; D'Amore, M.; Thakur, A.; Chammingkwan, P.;
811 Bruzzese, P. C.; Terano, M.; Civalleri, B.; Bordiga, S.; Groppo, E.; Taniike, T., Revisiting
812 the identity of δ-MgCl2: Part I. Structural disorder studied by synchrotron X-ray total
813 scattering. *J. Catal.* **2020,** *385*, 76-86.

814 31. Gnanakumar, E. S.; Gowda, R. R.; Kunjir, S.; Ajithkumar, T.; Rajamohanan, P.;
815 Chakraborty, D.; Gopinath, C. S., MgCl2· 6CH3OH: A simple molecular adduct and its
816 influence as a porous support for olefin polymerization. *ACS Catalysis* **2013,** *3* (3), 303-311.

817 32. D'Amore, M.; Thushara, K. S.; Piovano, A.; Causà, M.; Bordiga, S.; Groppo, E.,
818 Surface Investigation and Morphological Analysis of Structurally Disordered MgCl2 and
819 MgCl2/TiCl4 Ziegler–Natta Catalysts. *ACS Catal.* **2016,** *6* (9), 5786–5796.

820 33. Takasao, G.; Wada, T.; Thakur, A.; Chammingkwan, P.; Terano, M.; Taniike, T.,
821 Machine Learning-Aided Structure Determination for TiCl4–Capped MgCl2 Nanoplate of
822 Heterogeneous Ziegler–Natta Catalyst. *ACS Catal.* **2019,** *9* (3), 2599-2609.

823 34. Rytter, E.; Nirisen, O.; Ystenes, M.; Oye, H. A., FFIR Spectroscopy of Ethyl
824 Benzoate-Titanium Tetrachloride Complexes with Application to Supported Ziegler-Natta
825 Catalysts. *Mikrochim. Acta* **1988,** *II*, 85-87.

826 35. Sacchi, M. C.; Forlini, F.; Tritto, I.; Locatelli, P., Stereochemistry of the initiation step
827 in Ziegler-Natta catalysts containing dialkyl propane diethers: a tool for distinguishing the role
828 of internal and external donors. *Macromolecular Symposia* **1995,** *89*, 91-100.

829 36. Flisak, Z., Multidentate Tetrahydrofurfuryloxide Ligand in a Ziegler−Natta Catalyst
830 Studied by Molecular Modeling. *Macromolecules* **2008,** *41* (19), 6920-6924.

831 37. Grau, E.; Lesage, A.; Norsic, S.; Copéret, C.; Monteil, V.; Sautet, P., Tetrahydrofuran
832 in TiCl4/THF/MgCl2: a Non-Innocent Ligand for Supported Ziegler–Natta Polymerization
833 Catalysts. *ACS Catal.* **2013,** *3* (1), 52-56.

834 38. Wada, T.; Taniike, T.; Kouzai, I.; Takahashi, S.; Terano, M., Propylene
835 Polymerization Performance of Isolated and Aggregated Ti Species Studied Using a Well-
836 Designed TiCl3/MgCl2 Ziegler-Natta Model Catalyst. *Macromol. Rapid Commun.* **2009,** *30*
837 (11), 887-891.

838 39. Thakur, A.; Chammingkwan, P.; Wada, T.; Onishi, R.; Kamimura, W.; Seenivasan,
839 K.; Terano, M.; Taniike, T., Solution-state NMR study of organic components of industrial

Ziegler-Natta catalysts: Effect of by-products on catalyst performance. *Appl. Catal. A Gen.* **2021,** *611*, 117971.

40. Jeong, Y.-t.; Lee, D.-h.; Soga, K., Propene polymerization with Mg(OC2H5)2-supported TiCl4 catalyst, 2. Effects of TiCl4 treatment. *Makromol. Chem., Rapid Commun.* **1991,** *12* (1), 5-7.

41. Kim, I.; Choi, H. K.; Han, T. K.; Woo, S. I., Polymerization of propylene catalyzed over highly active and stereospecific catalysts synthesized with Mg(OEt)2/benzoyl chloride/TiCl4. *J. Polym. Sci. A Polym. Chem.* **1992,** *30* (10), 2263-2271.

42. Chumachenko, N. N.; Zakharov, V. A.; Bukatov, G. D.; Sergeev, S. A., A study of the formation process of titanium–magnesium catalyst for propylene polymerization. *Appl. Catal. A: Gen.* **2014,** *469*, 512-516.

43. Piovano, A.; D'Amore, M.; Wada, T.; Bruzzese, P. C.; Takasao, G.; Thakur, A.; Chammingkwan, P.; Terano, M.; Civalleri, B.; Bordiga, S.; Taniike, T.; Groppo, E., Revisiting the identity of δ-MgCl2: Part II. Morphology and exposed surfaces studied by vibrational spectroscopies and DFT calculation. *J. Catal.* **2020,** *387*, 1-11.

44. Taniike, T.; Funako, T.; Terano, M., Multilateral characterization for industrial Ziegler-Natta catalysts toward elucidation of structure-performance relationship. *J. Catal.* **2014,** *311*, 33-40.

45. Chammingkwan, P.; Terano, M.; Taniike, T., High-Throughput Synthesis of Support Materials for Olefin Polymerization Catalyst. *ACS Comb. Sci.* **2017,** *19* (5), 331-342.

46. Wada, T.; Funako, T.; Chammingkwan, P.; Thakur, A.; Matta, A.; Terano, M.; Taniike, T., Structure-performance relationship of Mg(OEt)2-based Ziegler-Natta catalysts. *J. Catal.* **2020,** *389*, 525-532.

863 47. Kohara, S.; Itou, M.; Suzuya, K.; Inamura, Y.; Sakurai, Y.; Ohishi, Y.; Takata, M.,
864 Structural studies of disordered materials using high-energy x-ray diffraction from ambient to
865 extreme conditions. *J. Phys.: Condens. Matter* **2007,** *19* (50), 506101.

866 48. Lorch, E., Neutron diffraction by germania, silica and radiation-damaged silica glasses.
867 *J. Phys. C: Solid State Phys.* **1969,** *2* (2), 229-237.

868 49. Kaduk, J. A., Conventional and Eccentric Uses of Crystallographic Databases in
869 Practical Materials Identification Problems. *J. Res. Natl. Inst. Stand. Technol.* **1996,** *101* (3),
870 281-294.

871 50. Tanase, S.; Katayama, K.; Inasawa, S.; Okada, F.; Yamaguchi, Y.; Sadashima, T.;
872 Yabunouchi, N.; Konakazawa, T.; Junke, T.; Ishihara, N., New Synthesis Method Using
873 Magnesium Alkoxides as Carrier Materials for Ziegler-Natta Catalysts with Spherical
874 Morphology. *Macromol. React. Eng.* **2008,** *2* (3), 233-239.

875 51. Chammingkwan, P.; Terano, M.; Taniike, T., High-Throughput Synthesis of Support
876 Materials for Olefin Polymerization Catalyst. *ACS Combinatorial Science* **2017,** *19* (5), 331-
877 342.

878 52. Wada, T.; Funako, T.; Chammingkwan, P.; Thakur, A.; Matta, A.; Terano, M.;
879 Taniike, T., Structure-performance relationship of Mg (OEt) 2-based Ziegler-Natta catalysts.
880 *Journal of Catalysis* **2020,** *389*, 525-532.

881 53. Egami, T.; Billinge, S. J. L., *Underneath the Bragg peaks: structural analysis of*
882 *complex materials*. Pergamon: 2003.

883 54. Benmore, C. J.; Alderman, O. L. G.; Robinson, D.; Jennings, G.; Tamalonis, A.;
884 Ilavsky, J.; Clark, E.; Soignard, E.; Yarger, J. L.; Weber, J. K. R., Extended range X-ray pair
885 distribution functions. *Nucl. Instrum. Methods Phys. Res. A* **2020,** *955*, 163318.

886 55. Vittadello, M.; Stallworth, P. E.; Alamgir, F. M.; Suarez, S.; Abbrent, S.; Drain, C.
887 M.; Di Noto, V.; Greenbaum, S. G., Polymeric δ-MgCl2 nanoribbons. *Inorganica chimica*
888 *acta* **2006,** *359* (8), 2513-2518.

889 56. Auriemma, F.; De Rosa, C., Theoretical investigation of (MgCl2) x polynuclear species
890 formed during preparation of MgCl2-supported Ziegler–Natta catalysts from solid solvates.
891 *Journal of Applied Crystallography* **2008,** *41* (1), 68-82.

892 57. Proffen, T.; Neder, R., DISCUS: A program for diffuse scattering and defect-structure
893 simulation. *Journal of applied crystallography* **1997,** *30* (2), 171-175.

894 58. Farrow, C.; Juhas, P.; Liu, J.; Bryndin, D.; Božin, E.; Bloch, J.; Proffen, T.; Billinge,
895 S., PDFfit2 and PDFgui: computer programs for studying nanostructure in crystals. *Journal of*
896 *Physics: Condensed Matter* **2007,** *19* (33), 335219.

897 59. Olds, D.; Wang, H.-W.; Page, K., DShaper: an approach for handling missing low-Q
898 data in pair distribution function analysis of nanostructured systems. *Journal of Applied*
899 *Crystallography* **2015,** *48* (6), 1651-1659.

900 60. Di Noto, V.; Zannetti, R.; Viviani, M.; Cecchin, G., Magnesium chloride-supported
901 catalysts for Ziegler-Natta propene polymerization: Ethyl formate as internal base. *Macromol.*
902 *Chem. Phys.* **1994,** *195* (10), 3395-3409.

903 61. Di Noto, V.; Lavina, S.; Longo, D.; Vidali, M., A novel electrolytic complex based on
904 δ-MgCl2 and poly(ethylene glycol) 400. *Electrochim. Acta* **1998,** *43* (10), 1225-1237.

905 62. Ferraro, J. R., *Low-frequency vibrations of inorganic and coordination compounds*.
906 Plenum Press: New York (US), 1971.

907 63. Finnie, K. S.; Luca, V.; Moran, P. D.; Bartlett, J. R.; Woolfrey, J. L., Vibrational
908 spectroscopy and EXAFS study of Ti(OC2H5)4 and alcohol exchange in Ti(iso-OC3H7)4. *J.*
909 *Mater. Chem.* **2000,** *10* (2), 409-418.

910 64. D'Amore, M.; Credendino, R.; Budzelaar, P. H. M.; Causá, M.; Busico, V., A periodic
911 hybrid DFT approach (including dispersion) to MgCl2-supported Ziegler–Natta catalysts – 1:
912 TiCl4 adsorption on MgCl2 crystal surfaces. *J. Catal.* **2012,** *286*, 103−110.

913 65. Puhakka, E.; Pakkanen, T. T.; Pakkanen, T. A., Theoretical investigations on Ziegler-
914 Natta catalysis: models for the interactions of the TiCl4 catalyst and the MgCl2 support. *Surf.*
915 *Sci.* **1995,** *334* (1), 289-294.

916 66. Taniike, T.; Terano, M., Coadsorption model for first-principle description of roles of
917 donors in heterogeneous Ziegler-Natta propylene polymerization. *J. Catal.* **2012,** *293*, 39-50.

918 67. Cheng, R. H.; Luo, J.; Liu, Z.; Sun, J. W.; Huang, W. H.; Zhang, M. G.; Yi, J. J.;
919 Liu, B. P., Adsorption of TiCl4 and electron donor on defective MgCl2 surfaces and propylene
920 polymerization over Ziegler-Natta catalyst: A DFT study. *Chinese J. Polym. Sci.* **2013,** *31* (4),
921 591-600.

922 68. Jung, H. S.; Lee, J.-K.; Kim, J.-Y.; Hong, K. S., Crystallization behaviors of nanosized
923 MgO particles from magnesium alkoxides. *J. Colloid Interface Sci.* **2003,** *259* (1), 127-132.

924 69. Rywak, A. A.; Burlitch, J. M.; Loehr, T. M., Sol-Gel Preparation and Characterization
925 of Magnesium Peroxide, Magnesium Hydroxide Methoxide, and Randomly and (111) Oriented
926 MgO Thin Films. *Chem. Mater.* **1995,** *7* (11), 2028-2038.

927 70. Interestingly, even the slope of the spectra baseline changes from A and B to the other
928 intermediates: since the baseline in the IR spectra is correlated with the scattering properties of

929 the particles, such a change can be interpreted as a contraction of the nanocrystals aggregates,
930 which gives rise to the interparticle porosity.

931 71. Potapov, A. G.; Bukatov, G. D.; Zakharov, V. A., DRIFT Study of Internal Donors in
932 Supported Ziegler-Natta Catalysts. *J. Mol. Catal. A: Chem.* **2006,** *246* (1-2), 248-254.

933 72. Cheruvathur, A. V.; Langner, E. H. G.; Niemantsverdriet, J. W.; Thüne, P. C., In Situ
934 ATR-FTIR Studies on MgCl2-Diisobutyl Phthalate Interactions in Thin Film Ziegler-Natta
935 Catalysts. *Langmuir* **2012,** *28* (5), 2643-2651.

936 73. Singh, G.; Kaur, S.; Makwana, U.; Patankar, R. B.; Gupta, V. K., Influence of Internal
937 Donors on the Performance and Structure of MgCl2 Supported Titanium Catalysts for
938 Propylene Polymerization. *Macromol. Chem. Phys.* **2009,** *210* (1), 69-76.

939 74. Potapov, A. G.; Bukatov, G. D.; Zakharov, V. A., DRIFTS Study of the Interaction of
940 the Internal Donor in TiCl4/di-n-Butyl Phthalate/MgCl2 Catalysts with AlEt3 Cocatalyst. *J.*
941 *Mol. Catal. A: Chem.* **2010,** *316* (1-2), 95-99.

942 75. Arzoumanidis, G. G.; Karayannis, N. M., Infrared spectral characterization of
943 supported propene polymerization catalysts: A link to catalyst performance. *Appl. Catal.* **1991,**
944 *76* (2), 221-231.

945 76. Makwana, U.; Naik, D. G.; Singh, G.; Patel, V.; Patil, H. R.; Gupta, V. K., Nature of
946 Phthalates as Internal Donors in High Performance MgCl2 Supported Titanium Catalysts.
947 *Catal. Lett.* **2009,** *131* (3), 624-631.

948 77. Yang, C. B.; Hsu, C. C.; Park, Y. S.; Shurvell, H. F., Infrared characterization of
949 MgCl2 supported Ziegler-Natta catalysts with monoester and diester as a modifier. *Eur. Polym.*
950 *J.* **1994,** *30* (2), 205-214.

951 78. Kissin, Y. V.; Liu, X.; Pollick, D. J.; Brungard, N. L.; Chang, M., Ziegler-Natta
952 catalysts for propylene polymerization: Chemistry of reactions leading to the formation of
953 active centers. *J. Mol. Catal. A: Chem.* **2008,** *287* (1), 45-52.

954 79. Stukalov, D. V.; Zakharov, V. A.; Potapov, A. G.; Bukatov, G. D., Supported Ziegler-
955 Natta catalysts for Propylene Polymerization. Study of Surface Species Formed at Interaction
956 of Electron Donors and TiCl4 with Activated MgCl2. *J. Catal.* **2009,** *266* (1), 39-49.

957 80. Shetty, S., Synergistic, reconstruction and bonding effects during the adsorption of
958 internal electron donors and TiCl4 on MgCl2 surface: A periodic-DFT investigation. *Surf. Sci.*
959 **2016,** *653*, 55-65.

960 81. This method is actually only semi-quantitative because it does not take into account the
961 different extinction coefficients of the absorption bands.

962 82. Cavallo, L.; Ducéré, J. M.; Fedele, R.; Melchior, A.; Mimmi, M. C.; Morini, G.;
963 Piemontesi, F.; Tolazzi, M., Ziegler-Natta catalytic systems. *J. Therm. Anal. Chem.* **2008,** *91*
964 (1), 101-106.

965 83. Credendino, R.; Minenkov, Y.; Liguori, D.; Piemontesi, F.; Melchior, A.; Morini,
966 G.; Tolazzi, M.; Cavallo, L., Accurate experimental and theoretical enthalpies of association
967 of TiCl4 with typical Lewis bases used in heterogeneous Ziegler-Natta catalysis. *Phys. Chem.*
968 *Chem. Phys.* **2017,** *19* (39), 26996-27006.

969 84. Piovano, A.; D'Amore, M.; Thushara, K. S.; Groppo, E., Spectroscopic Evidences for
970 TiCl4/Donor Complexes on the Surface of MgCl2-Supported Ziegler-Natta Catalysts. *Journal*
971 *of Physical Chemistry C* **2018,** *122* (10), 5615-5626.

85. Kuklin, M. S.; Bazhenov, A. S.; Denifl, P.; Leinonen, T.; Linnolahti, M.; Pakkanena, T. A., Stabilization of magnesium dichloride surface defects by mono- and bidentate donors. *Surf. Sci.* **2015,** *635*, 5–10.

86. Brisdon, B. J.; Lester, T. E.; Walton, R. A., Complex halides of transition metals—III electronic absorption spectra of hexahalotitanates(IV), vanadates(IV), and zirconates(IV). *Spectrochim. Acta A* **1967,** *23* (7), 1969-1976.

87. Jorgensen, C. K., Electron Transfer Spectra. *Progr. Inorg. Chem.* **1970,** *12*, 101-157.

88. Jorgensen, C. K., Electronegativity and Chemical Bonding. In *Orbitals in Atoms and Molecules*, Academic Press: London and New York, 1962; pp 80-100.

89. Piovano, A.; Pletcher, P.; Velthoen, M. E. Z.; Zanoni, S.; Chung, S.-H.; Bossers, K.; Jongkind, M. K.; Fiore, G.; Groppo, E.; Weckhuysen, B. M., Genesis of MgCl2-based Ziegler-Natta Catalysts as Probed with Operando Spectroscopy. *ChemPhysChem* **2018,** *19* (20), 2662-2671.

90. Seenivasan, K.; Sommazzi, A.; Bonino, F.; Bordiga, S.; Groppo, E., Spectroscopic Investigation of Heterogeneous Ziegler-Natta Catalysts: Ti and Mg Chloride Tetrahydrofuranates, Their Interaction Compound, and the Role of the Activator. *Chemistry a European Journal* **2011,** *17* (31), 8648-8656.

91. Piovano, A.; Morra, E.; Chiesa, M.; Groppo, E., Tuning the Ti3+ and Al3+ Synergy in an Al2O3/TiClx Catalyst to Modulate the Grade of the Produced Polyethylene. *ACS Catal.* **2017,** *7* (8), 4915-4921.

92. Piovano, A.; Signorile, M.; Braglia, L.; Torelli, P.; Martini, A.; Wada, T.; Takasao, G.; Taniike, T.; Groppo, E., Electronic Properties of Ti Sites in Ziegler–Natta Catalysts. *ACS Catalysis* **2021,** *11* (15), 9949-9961.

995 93. Vittoria, A.; Antinucci, G.; Zaccaria, F.; Cipullo, R.; Busico, V., Monitoring the
996 Kinetics of Internal Donor Clean-up from Ziegler–Natta Catalytic Surfaces: An Integrated
997 Experimental and Computational Study. *The Journal of Physical Chemistry C* **2020,** *124* (26),
998 14245-14252.

999 94. Momma, K.; Izumi, F., VESTA 3 for three-dimensional visualization of crystal,
1000 volumetric and morphology data. *Journal of applied crystallography* **2011,** *44* (6), 1272-1276.

1001

1002

1003 Table of Contents graphic

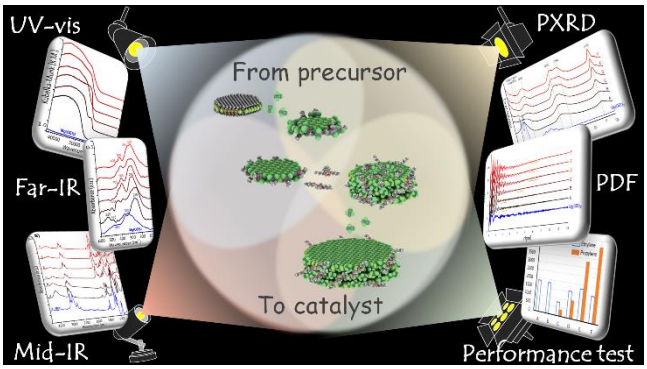

1004